Laser Derived Electron Transport Layers with Embedded p-n Heterointerfaces Enabling Planar Perovskite Solar Cells with Efficiency over 25%

Wenhao Zhao[#], Pengfei Guo[#], Chen Liu, Ning Jia, Zhiyu Fang, Linfeng Ye, Qian Ye, Yadong Xu, Aleksandr P. Glotov, Andrei A. Novikov, Vladimir A. Vinokurov, Dmitry Shchukin and Hongqiang Wang[*]

W. Zhao, Dr. P. Guo, C. Liu, N. Jia, Z. Fang, L. Ye, Dr. Q. Ye, Prof. Y. Xu, Prof. H. Wang
State Key Laboratory of Solidification Processing, Center for Nano Energy Materials, School of Materials Science and Engineering, Northwestern Polytechnical University and Shaanxi Joint Laboratory of Graphene (NPU), Xi'an, 710072, P. R. China
E-mail: hongqiang.wang@nwpu.edu.cn
Dr. P. Guo, Prof. H. Wang
Chongqing Innovation Center of Northwestern Polytechnical University, Northwestern Polytechnical University, Chongqing, 401135, China
Prof. Y. Xu,
Northwestern Polytech Univ, State Key Lab Solidification Proc, MIIT Key Lab Radiation Detect Mat & Devices, Xian 710072, P. R. China
Dr. A. P. Glotov, Dr. A. A. Novikov, Prof. V. A. Vinokurov
Gubkin Russian State University of Oil and Gas, Gubkin University, 19991, Moscow, 65/1 Leninskiy Ave., Russia
Prof. D. Shchukin
Stephenson Institute for Renewable Energy, University of Liverpool, Liverpool L69 7ZF, UK
[#] These authors contribute equally to this work.

Abstract

Electron transport layers (ETLs) with pronounced electrons conducting capability are of essential for high performance planar photovoltaics, while this has been posing great challenges for the most widely used metal oxide ETLs that are featured unfortunately with intrinsic low carriers mobility. We herein demonstrate that by simply addressing the carriers loss at particle boundaries of TiO_2 ETLs through embedding in ETL p-n heterointerfaces, the electrons mobility of the ETLs can be boosted as high as three orders of magnitude. Such embedding was also found encouragingly favorable for inhibiting the formation of rutile phase TiO_2 in ETL, as well as initiating the growth of the on top high-quality and large-grain perovskite films with less defect states. By virtue of these merits, we achieve in present study formamidinium lead iodide PSCs with a champion efficiency of 25.05%, setting a new benchmark for plannar PSCs employing TiO_2 ETLs. Unencapsulated PSCs employing such ETLs deliver also much-improved environmental stability, i.e., more than 80% of their initial efficiency after 9000 h of air storage under RH of 40%, and over 90% of their initial efficiency at maximum power point under continuous illumination for 500 h. Further work exploring other laser generated p-type nanocrystals for embedding warrants the proposed strategy a universal alternative for addressing the low carriers mobility of metal oxide based ETLs from the view point of particle boundaries engineering.

Keywords: electrons transport layer, p-n heterointerfaces, electron mobility, particle boundaries, perovskite solar cells

Introduction

Planar halide perovskite solar cells (PSCs) have been attracting increased interests owing to their potentials on low-cost construction of high performance tandem and/or flexible photovoltaics.[1-2] In addition to the important photoactive perovskite layer that absorbs incident photons to generate sufficient photogenerated carriers, the planar PSCs necessitate the electron transport layer (ETL) that plays crucial roles not only on efficiently extracting and conducting the photogenerated electrons to the out circuit,[3] but also elaborately ruling the growth of the on-top high quality halide perovskite.[4] Compact films of metal oxides such as TiO_2, ZnO, SnO_2, and La-$BaSnO_3$ have been widely explored as efficient ETLs due to their ease solution-processing that is compatible with the low-cost and low-temperature processing of the perovskite layer.[5] As one of the most important ETLs that is traditionally used in dye-sensitized solar cells,[6] TiO_2 is screened as the most widely adopted ETL in regular planar PSCs owing to its high optical transmittance and excellent thermal stability, low cost as well as suitable energy level.[7] With the intensive efforts devoted on the engineering of TiO_2 ETL in planar PSCs, the power conversion efficiency (PCE) could reach a benchmark value as high as 24.8%, which unfortunately still lags behind the efficiency of PSCs employing SnO_2 as ETL.[8] The reason behind such efficiency gap is largely due to the insufficient electrons conducting capability of the TiO_2 ETL, which principally accounts for the electron accumulation at the buried interface and the unbalanced carrier transport within PSCs, thus leading to the unsatisfied *I-V* hysteresis, less-than-ideal PCE and light-induced instability.[9-10] Encouragingly, the intrinsic low carriers mobility of the TiO_2 nanoparticles (usually at the level of 10^{-5}~10^{-4} $cm^2V^{-1}s^{-1}$) in the ETLs has recently been intensively addressed by several state-of-art engineering strategies, exemplified by a high-quality single-crystalline TiO_2 nanoparticles based ETL with the electron mobility as high as 6.04 $cm^2V^{-1}s^{-1}$, as well as the nitrogen-doped TiO_2 ETL with an increased electrons mobility up to 0.5 $cm^2V^{-1}s^{-1}$ that leads to the PSC with a fill factor >86%.[11-12] While noting that TiO_2 ETL is essentially a layer composed of stacked TiO_2 nanoparticles, the inhibition of carriers loss at the particle boundaries (PBs) in between adjacent nanoparticles of ETL should be considered as equally important as improving the intrinsic carriers mobility of the nanoparticles, as described in Schemes 1a and 1b.[13] Inspired by the grain boundaries engineering of the polycrystalline perovskite films that could alleviate the defect trap states and modulate the carriers dynamics, it would thus be highly promising to improve the electron mobility of TiO_2 based ETLs by addressing the carriers loss at PBs for highly efficient and stable planar PSCs.

Herein, we demonstrate an effective strategy of PBs engineering via laser embedding p-n heterointerfaces at ETLs, which could enable boosted electrons mobility of TiO_2 ETL by maximally three

orders of magnitude, thus results in a planar PSC with a new benchmark PCE over 25%. By virtue of the unique advantage of pulsed laser irradiation in liquid on producing well defined nanocrystals in desired solvents, we are able to embed laser generated p-type nanocrystals at the PBs of the n-type TiO_2 ETLs. The embedded p-n heterointerfaces could efficiently inhibit the carrier loss at PBs owing to not only the elimination of the electrons trapping at TiO_2 nanoparticles but also boosted electrons transfer between adjacent TiO_2 nanoparticles through localized built-in electric filed (Scheme 1c). By elaborately modulating the amount of embedded p-type CdTe nanocrystals, the electrons mobility of ETLs could be enhanced from 2.67×10^{-5} up to 1.89×10^{-2} $cm^2V^{-1}s^{-1}$. The embedding of CdTe nanocrystals were found also helpful to modulate the crystallization kinetics of TiO_2 matrix, which was verified favorable for the inhibition of rutile TiO_2 that is detrimental for the electrons conducting and light induced stability of perovskite. Owing to the boosted electrons conducting at ETL and subsequent suppressing of charge accumulation and recombination at the interface between ETL and perovskite, we achieve in present study highly efficient formamidinium lead iodide PSCs with a top record efficiency of 25.05%, which is as far as we know the highest value among TiO_2-based planar PSCs. The novel TiO_2@CdTe ETL was found helpful to initiate high-quality and large-grain perovskite films with reduced interfacial defects, leading to the construction of the mixed-cation PSCs with stable shelf storage over 9000 h (moisture RH of 40%), and $FAPbI_3$ PSCs that could maintain over 90% of their initial efficiency at maximum power point under continuous illumination for 500 h. We believe this study provides an efficient alternative of improving the carriers mobility of charge transport layer for high performance planar PSCs from the view point of PBs engineering.

Results

Embedding laser-generated p-type CdTe nanocrystals in TiO_2 ETL.

In order to locate the p-type nanocrystals at the PBs of TiO_2 ETL, we first use the technology of pulsed laser irradiation in liquid to generate size controlled CdTe nanocrystals (Figure 1a) in the precursor solvent used for chemical bath deposition of TiO_2 ETL. By optimizing the processing parameters such as laser fluence, irradiation time and cooling temperature (Figure S1, Supporting Information), a stable and well-dispersed p-type CdTe nano-colloids showing Mie-scattering and with an average size of 3 nm were consequently obtained, as illustrated in Figure 1b. High resolution transmission electron microscopy (HRTEM) was employed to determine the crystal structure of the as-prepared CdTe nanocrystals. The lattice fringes with a spacing of 0.37 nm shown in Figure 1c are affiliated to the characteristic plane (111) of CdTe, which is further evidenced by the corresponding fast Fourier transform (FFT) of selected area that shows (111) and (311) plane with 29.5°

included angle. Similar results towards larger nanoparticles were also acquired and further confirmed by Raman spectroscopy (Figures S2-3, Supporting Information), indicating that there is no significant crystalline change in CdTe during laser irradiation. Furthermore, the elements mapping determined by TEM-energy dispersive spectroscopy (TEM-EDS) suggests homogeneous distributions of all elements throughout both nanoparticles and nanocrystals without elements segregation during laser process (Figure S4, Supporting Information), consistent with the analyses of the X-ray photoelectron spectroscopy (XPS, Figure S5, Supporting Information).

Subsequent to the acquiring of CdTe nanocrystals in the precursor solvent for depositing TiO_2, a facile one-step chemical bath co-deposition approach is adopted for *in situ* embedding laser generated sub-10 nm CdTe nanocrystals (Figure 1a and Figure S6, Supporting Information). In brief, different amounts (3%, 6% and 9% volume ratio to $TiCl_4$ precursor abbreviated as 3%-CdTe-TiO_2, 6%-CdTe-TiO_2, 9%-CdTe-TiO_2) of CdTe colloids solution with 0.1 mg/ml concentration were added to the $TiCl_4$ precursor for construction of ETL. The surface morphologies of the TiO_2 ETL with or without embedding of CdTe nanocrystals were evaluated by scanning electron microscopy (SEM) and atomic force microscopy (AFM). Compared with the pristine TiO_2, CdTe@TiO_2 exhibits more smoother surface with reduced roughness from 31.0 nm to 12.1 nm (Figures 1f-g, Figures S7-8, Supporting Information). As it was reported that the embedding of laser generated nanocrystals at the grain boundaries of perovskite could in principle alter the crystalline kinetics of the matrix, we collected the predicated TiO_2 powder after the co-deposition for further XRD analysis to investigate if the embedding of CdTe nanocrystals could influence the crystallization kinetics of TiO_2. As shown in Figure 1d, the obtained TiO_2 without embedding of CdTe exhibits a polymorphic phase including rutile and anatase in the range of temperature from 30 to 150 °C. By contrast, the rutile phase is remarkably restrained after embedding CdTe nanocrystals, as shown in Figure 1e.

Generally, anatase phase is easily formed with fast nucleation rate during the hydrolysis of $TiCl_4$, whereas slow nucleation rate facilitates directional arrangement of aggregates and formation of more stable rutile phase.[14] We thus deduce that the incorporation of CdTe nanocrystals could initiate the crystal nucleation and speed up the crystallization of TiO_2, since more nanocrystals in the starting precursor result in the formation of more nuclei at the beginning of hydrolysis process and thus smaller TiO_2 nanocrystals, which favors dispersion of TiO_2 nanocrystals in solvent and formation of compact anatase TiO_2 film.[9] This result is in agreement with the case of using nanocrystals in anti-solvent to modulate the crystalline kinetics of perovskite films. We believe such rapid crystallization induced inhibition of the rutile phase would be much favorable for

the construction of an ideal TiO_2 ETL in PSCs, not only because rutile phase TiO_2 has lower carrier mobility than that of anatase phase, but also due to the elimination of the mixed anatase-rutile TiO_2 with unfavorable photocatalysis property that are detrimental for the stability of PSCs upon AM 1.5 illumination.[15]

In order to confirm the existence of CdTe nanocrystals within the bulk TiO_2, cross-sectional TEM with EDS mapping is performed to probe spatial distribution of CdTe nanocrystals throughout the entire thickness. As shown in Figure 2a, the EDS mapping shows homogeneous distribution of CdTe nanocrystals within overall matrix due to well-dispersed CdTe nanocrystals in the $TiCl_4$ precursor (Figure S9, Supporting Information). The Cd and Te compositions do not change after embedding CdTe nanocrystals in TiO_2 matrix and retain atomic fraction ratio of 1:1 (Figure S10, Supporting Information). The cross-sectional HRTEM (Figure 2c from magnified red region of Figure 2b) convincingly demonstrates successful embedding by identifying typical lattice space of 0.35 nm and 0.37 nm that successively corresponds to (101) plane of TiO_2 and (111) plane of CdTe. Such embedding is further determined by corresponding fast Fourier transform (FFT) of selected area in Figure 2c, demonstrating (101) and (200) planes of TiO_2 with 21.7° plane included angle (Figure 2d), as well as (111) and (311) planes of CdTe with 29.5° angle (Figure 2e).

The UV-vis absorption spectra and corresponding Tauc plot were conducted to determine optical bandgap of ETLs upon CdTe embedding. It is found that embedding of CdTe nanocrystals causes slight change on the bandgap of TiO_2 ETL ranging from 3.20 to 3.23 eV, but negligible influence on the optical transmittance (Figures S11-12, Supporting Information). The space charge-limited current (SCLC) was adopted to evaluate the defect density (N_t) and charge mobility of different ETLs. The results exhibit an obvious reduction of N_t from pristine 3.95×10^{16} to 1.32×10^{16}, 0.97×10^{16} and 1.59×10^{16} cm^{-3} for 3%, 6%, 9%-CdTe-TiO_2 ETLs, respectively (Figure S13 and Table S1, Supporting Information), which could be attributed to the enhanced crystallinity from the embedded CdTe nanocrystals. Also, the electron mobilities (μ) were calculated to be 2.67×10^{-5}, 8.10×10^{-3}, 1.89×10^{-2} and 6.07×10^{-4} $cm^2\ V^{-1}\ s^{-1}$ for the pristine and 3%, 6%, 9%-CdTe-TiO_2 ETLs, respectively (Figure 2f, Note S1, Supporting Information), indicating a maximum increment of three orders of magnitude after the embedding of CdTe nanocrystals. Simultaneously, the conductivity (σ) of target ETL increases dramatically compared to that of pristine ETL, agreeing well with the mobility result (Figure S14, Supporting Information). The increased mobility and conductivity are probably ascribed to the formation of p-n heterojunction between TiO_2 and CdTe, in specific, p-type semiconductor feature of CdTe is confirmed by Ultraviolet photoelectron spectroscopy (UPS, Figure 2g) based on the optical bandgap (2.26 eV) (inset in Figure 2g), Fermi energy level (-3.92 eV), the calculated valence band value of -4.92 eV, and conduction band

value of -2.66 eV, respectively, reflected by an inverted "V-shape" Mott-Schottky plots shown in Figure 2h.[16]

Influence of embedding of CdTe in TiO_2 ETL on the top perovskite film.

We find that the embedding CdTe in TiO_2 ETL also plays a significant role on the surface morphology and grain sizes of the top perovskite films. Considering the improved surface smoothness of TiO_2 ETL upon CdTe embedding (Figures S8, Supporting Information), the contact angle measurement was further conducted to investigate the wettability of perovskite precursor on different TiO_2 substrates (Figure S15, Supporting Information). The result shows that the contact angles sharply decrease from 15º to 2º as the content of CdTe nanocrystals increases, favoring the reduction of Gibbs free energy for improved crystallization kinetics during the perovskite deposition.[10] As depicted in Figure 3a-b, the mixed-cation perovskite films with the composition of $Cs_{0.05}(FA_{0.85}MA_{0.15})_{0.95}PbI_{2.55}Br_{0.45}$ (CsFAMA) deposited on CdTe@TiO_2 ETL show smoother surface and larger grain size compared to those deposited on pristine TiO_2 ETL, further evidenced by the decreased RMS roughness from AFM characterization and improved crystallinity from XRD analyses (Figures S16-17, Supporting Information).

The steady-state photoluminescence (PL) and time-resolved PL (TRPL) spectra were employed to investigate the carrier dynamics between perovskite and ETL. As shown in Figure 3c, the PL intensity of perovskite films deposited on optimal CdTe@TiO_2 ETLs significantly decreases by about four times, manifesting more effective electron transport and extraction from perovskite to ETL. Meanwhile, the carrier lifetime of perovskite films upon all ETLs extracted from time-resolved photoluminescence (TRPL) spectra shows prominent decrease from 247.04 ns to 92.55 ns and 82.14 ns for the pristine TiO_2, 3%-CdTe-TiO_2 and 6%-CdTe-TiO_2, respectively (Figure 3d and Table S2, Supporting Information). The result reveals suppressive charge accumulation and enhanced electron extraction and transport at the buried interface.[17] We proceeded to conduct electrical impedance spectroscopy (EIS) to probe interface carrier transport behavior within the device. The result shows the decrease of the contact resistance *R*co values from 27159 Ω to 2422 Ω, and the increment of the recombination resistance *R*rec values from 1.47×10^5 to 3.11×10^5 after embedding nanocrystals, indicating improved charge transport and effectively suppressed charge recombination at the buried interface (Figures 3i and S18, Table S3, Supporting Information).[18]

Subsequently, it was found that the embedding of CdTe also favors for the effectively restrained leakage current from carrier recombination by dark current evaluation, as well as higher built-in potential (V_{bi}) enabling improved open-circuit voltage (*V*oc) output by capacitance-voltage (*C-V*) measurement of targe devices (Supplementary Figure S19, Figure S22c, Supporting Information). This is attributed to more efficient charge

extraction for restrained recombination caused by serious electron accumulation, and better energy level alignment between CdTe embedded TiO_2 and perovskite due to the upward shifts of TiO_2 work function by the embedded p-n heterointerfaces for reduced the interface barrier, as proved by UPS result (Figure 3j, Note S2 and Figures S20-21, Supporting Information).[7]

We further found that embedding of CdTe nanocrystals has important effects on tuning the defects in the perovskite absorber, which was confirmed by the temperature dependent admittance spectroscopy (TAS) combined with Mott-Schottky analysis (Note S3, Supporting Information). The capacitance-frequency (*C-f*) curves of different devices were measured at various temperature (210-330K) under dark to calculate their defect activation energies (*E*a) to be 0.252 and 0.219 eV, respectively (Figure 3e, Figure S22a-b, Supporting Information). The trap density-of-states distribution and their energy levels are presented in Figure 3f, indicating that such embedding effectively decreases the energy level of trap states from 0.15 to 0.12 eV, as well as their density of states from 2.22×10^{16} to 1.24×10^{16} cm^{-3} eV^{-1}. In addition to the improved crystallinity of perovskite film on CdTe@TiO_2 ETL, we also ascribe such considerable decrease of N_t for perovskite films to suppression of interfacial iodine vacancy arising from the interaction between CdTe and perovskite, i.e. the binding of Cd^{2+} and iodine ions as well as under-coordinated Pb^{2+} defects by Cd^{2+}(O).[19] This was experimentally verified by the XPS analysis of the product after mixing laser generated CdTe and PbI_2, as shown in Figure 3g, where the Cd $3d_{3/2}$ was assigned to four peaks at 410.7, 412.1, 413.6 and 415.5 eV corresponding to Cd^{2+}(O), Cd-Te, Cd-I and Cd^{2+} (complex), respectively.[19] The peaks of I $3d_{3/2}$ can be fitted to two peaks at 630.7 and 632.0 eV belong to the bands of I-Pb and I-Cd that results from the interaction between Cd^{2+} and iodine for preventing iodine ions from migrating, reflected from disappearance of metallic Pb (Figure 3h and Figures S23-24, Supporting Information).[20]

Photovoltaic performance of planar PSCs employing CdTe@TiO_2 ETLs.

The regular planar PSCs with the configuration of FTO substrate/CdTe@TiO_2/perovskite/Spiro-OMeTAD/Au were fabricated to confirm the effect of CdTe nanocrystals embedding on photovoltaic performance (Figure S25, Supporting Information). The detailed fabrication process of device is shown in Figure S26, Supporting Information. Figure 4a shows the current density-voltage (*J-V*) curves of different CsFAMA-based champion devices measured under illumination of 100 mW/cm^2 (AM 1.5G) and the photovoltaic parameters were summarized in Table 1. The device upon 6%-CdTe-TiO_2 layer achieved the champion PCE up to 22.00% with *V*oc of 1.191 V, short-circuit current density (J_{SC}) of 23.76 mA/cm^2 and fill factor (FF) of 77.74%, which far exceeds those of pristine TiO_2 (20.05%), 3%-CdTe-TiO_2 (21.68%) and 9%-

CdTe-TiO_2 (20.98%) based devices. Moreover, champion device shows negligible hysteresis (hysteresis factor: 0.9%) and a stabilized PCE of 21.94% close to champion efficiency, in contrast with that of control (12.8%) (Figure 4b and Table S4, Supporting Information). To further confirm the roles of laser embedding of CdTe nanocrystals for their enhanced photovoltaic performance, we constructed pure α-phase $FAPbI_3$ absorber based PSCs. It was found that target $FAPbI_3$ PSCs exhibit optimized morphology with larger grain throughout the entire thickness of film, perfect crystallinity orientation along the direction perpendicular to the substrate as well as improved interfacial carrier dynamics (Figures S27-31, and Table S5, Supporting Information). Encouragingly, we acquire a champion device delivering the efficiency of 25.05% (stabilized power output: 24.91%) with *V*oc of 1.167 V, J_{SC} of 25.61 mA/cm^2 and fill factor (FF) of 83.81%, a maximum 10% PCE enhancement relative to control (22.72%, a band gap of 1.53 eV), as shown in Figure 4c and Figure S32, Supporting Information. As shown in Figure 4d, the enhancement of EQE response in the entire range is attributed to the compact and large grains of perovskite film grown on CdTe nanocrystals embedded ETLs,[21] resulting in improved *J*sc from 24.06 and 25.11 mA/cm^2 for control and target devices, respectively, which agree well with the *J*sc values from *J-V* results. The highly stabilized PCE demonstrated that devices embedded by CdTe nanocrystals enable suppression of ion migration, as illustrated by better alignment of the logarithmic *I-V* plots under contrast sweep direction (Figure 4e).[22] Meanwhile, a histogram of 50 individual devices based different perovskite suggests that average PCE are improved from 18.95±0.73% to 21.23±0.49% and from 21.36±1.29% to 23.81±0.85%, respectively, as well as the enhancement of *V*oc, *J*sc and FF (Figure 4f, Table 1 and Figures S33-34, Supporting Information).

Owing to the improved crystallinity and decreased defect states of perovskite films on CdTe@TiO_2 ETLs, we further evaluate the effect of CdTe emdedding in ETL on environmental stability of PSCs. As shown in Figure 4g, the long-term humidity durability of all unencapsulated CsFAMA-based devices was examined under 40% relative humidity (RH) in the dark at room temperature. The result shows that the target devices maintain almost 81% of initial PCE over 9000 h, whereas control devices degrade continuously to 42% after 1000 h. Likewise, the target devices exhibit excellent thermal and operational stability (Figure S35, Supporting Information). In view of the fact that $FAPbI_3$ perovskite has typical spontaneous phase-transition from α- to δ-$FAPbI_3$ under ambient atmosphere, we further examined the stability of $FAPbI_3$ based PSCs employing CdTe@TiO_2 ETLs. As shown in Figure S36, the humidity stability of unencapsulated target $FAPbI_3$ devices is significantly enhanced, retaining over 85% of initial efficiency for 1200 h under the RH of 30~40%, compared with that of control devices (less than 32%). The operational stability of $FAPbI_3$ devices was conducted by

maximum power point (MPP) tracking at 60 °C under 1 sun illumination in inner atmosphere (Figure 4h). After illumination of 200 h, the pristine $FAPbI_3$ device degrades to 68% of its initial PCE, whereas the nanocrystals embedded $FAPbI_3$ device maintains over 90% of its initial PCE for 500h. Such improved light stability could also be due to the prohibited formation of mixed anatase-rutile TiO_2 phases in ETLs owing to the inhibited rutile TiO_2 from CdTe induced fast crystallization of ETL (Figure 1e).

Discussion

It is worth noting that the embedding of CdTe nanocrystals has actually multifunctions for the improving of PSCs performance: i) embedded p-n heterointerfaces enable a remarkable increment of three orders of magnitude in the electron mobility of ETL (Table S6, Supporting Information), due to the synchronously eliminating of the carriers loss at the PBs of TiO_2 ETL and the electrons trapping at TiO_2 nanoparticles surface through localized built-in electric filed; ii) the introducing of CdTe nanocrystlas in the precursor solution of TiO_2 ETL could initiate the fast crystallization of TiO_2 film and thus inhibited rutile TiO_2 phase with slow nucleation rate, which accounts partially for the improved electrons mobility of ETL as well as light stability of PSCs employing CdTe@TiO_2 ETLs; iii) the increased smoothness and the improved wettability of CdTe@TiO_2 ETLs, as well as the synchronous passivation of interfacial under-coordinated Pb^{2+} by Cd^{2+}(O) and the reinforced anchoring effect of Cd^{2+} and iodine ions, favor for the construction of the top high-quality and large-grain perovskite with less defect states.[10,19] Benefiting from these desirable merits, a $FAPbI_3$ based PSC with the top record of PCE up to 25.05%, as well as a mixed-cation PSC with pronounced moisture stability (RH of 40%) over 9000 h were achieved. It could be deduced from significant improvement of all photovoltaic parameters that the increment in *V*oc, *J*sc and FF are due to better energy level alignment between perovskite and ETL and suppressed interfacial nonradiative recombination,[23] suitable energy gaps and efficient charge extraction,[24] as well as reduced contact resistance at the perovskite/ETL interfaces,[25-26] respectively. In particular, a negligible hysteresis shown in 6%-CdTe-TiO_2 based device is due to the removal of carrier transportation imbalance at both electrodes of the devices upon enhancement of electrical property of ETL. Furthermore, 0.1 mg/ml as the optimal concentration of laser embedding is proved from *J*-*V* results employing different concentration of CdTe nanocrystals (Figures S37, Table S7, Supporting Information)

In virtue of universal and unique features of pulsed laser irradiation on generating any nanocrystals in desired solvents, we further explore the embedding other laser generated p-type semiconductor nanocrystals into TiO_2 film for enhancing photovoltaic property of PSCs. Exemplified by the p-type GaAs, we prepared a transparent gallium arsenide (GaAs) colloidal solution with well-dispersed sub-10 nm nanocrystals (average

size: 3 nm) by laser irradiation. The Mie-scattering and the HRTEM image exhibits the labeled lattice fringes (0.33 nm) that correspond to the lattice spacing of GaAs (111) plane (Figure S38a, Supporting Information). The element mapping presents the stable existence for all elements whether nanoparticles or nanocrystals after laser irradiation, whereas nanocrystals present heterogeneous element distributions due to Ga oxide shell preferentially formed based on the lower oxidation Gibbs free energy of Ga than that of As (Figures S38b, Supporting Information).[27] The existence of GaAs nanocrystals in the TiO_2 film has been verified by SEM-EDS as well as corresponding elements mapping, (Figures S39a, Supporting Information). Likewise, the embedding of such nanocrystals contributes to more denser and smoother surface of TiO_2 and perovskite films than control, and observably improved μ from 2.67×10^{-5} to 1.08×10^{-2} $cm^2 V^{-1} s^{-1}$, as well as construction of p-n junction enabling the upward shift of TiO_2 work function with better energy level alignment with perovskite (Figures S39b-40, Supporting Information). Consequently, the initial attempts on construction of PSCs employing GaAs@TiO_2 ETLs yield CsFAMA-based device with improved PCE up to 21.54% with enhanced photovoltaic parameters, as well as $FAPbI_3$-based PSC with improved efficiency up to 23.49%, (Figures S41-42, Table S8, Supporting Information). Though the efficiency needs a substantial improvement comparing to the embedding of CdTe, we believe such attempt proves the universal feature of the strategy of embedding p-type nanocrystals at PBs of TiO_2 ETLs for addressing the unwanted carriers loss in metal oxides based ETLs, which would thus be inspiring for the design of efficient ETLs for high performance of PSCs with the planar configuration.

Conclusion

In summary, we have demonstrated an efficient strategy of boosting the electrons conducting capability of metal oxide based ETLs, which is of particularly importance for developing high performance planar PSCs. By generating well defined p-type CdTe nanocrystals in the precursor solvent of TiO_2 ETL, the nano-colloids were found helpful for regulating the crystallization kinetics of TiO_2 by inhibiting the rutile TiO_2 that is detrimental for the electrons conducting and light stability of the on top perovskite. The embedded p-n heterointerfaces are considered favorable not only for eliminating the electron trapping at TiO_2 nanoparticles surface and carrier loss at PBs, but also the upward shifts of TiO_2 work function with better energy level alignment with perovskite, thus resulting in an enhancement in voltage output and electron extraction. The increased smoothness and the improved wettability of CdTe@TiO_2 ETLs, also exert significant influence on the growth of high-quality perovskite films with larger grain size, lower defect density and improved crystallinity. We consequently achieved a top record efficiency of 25.05% for TiO_2 ETL based planar $FAPbI_3$

PSCs as well as highly stable CsFAMA PSCs with pronounced moisture stability (RH of 40%) over 9000 h. Owing to universal and unique property of pulsed laser irradiation, embedding other laser generated nanocrystals has been demonstrated to be general for effectively addressing the carriers loss in TiO_2 ETL. This study may provide a novel pathway of developing efficient ETLs for plannar PSCs based on laser-matter interactions.

Acknowledgements

W.Z. and P.G. contributed equally to this work. This work was financially supported by the project of the National Key R&D Program for International Cooperation (2021YFE0115100), the National Natural Science Foundation of China (52172101 and 52202115), the Shaanxi Science and Technology Innovation Team (2023-CX-TD-44), the China Postdoctoral Science Foundation (2022M722586), the Natural Science Foundation of Chongqing, China (CSTB2022NSCQ-MSX1085), Shaanxi Province Key Research and Development Program (2022KWZ-04 and 2021ZDLGY14-08), the Fundamental Research Funds for the Central Universities (3102019JC005 and and G2022KY0604). The authors would like to thank the Analytical & Testing Center of Northwestern Polytechnical University and Shaanxi Materials Analysis and Research Center for XPS, XRD, SEM and TEM characterizations.

References

[1] K. Xiao, Y.-H. Lin, M. Zhang, R. D. J. Oliver, X. Wang, Z. Liu, X. Luo, J. Li, D. Lai, H. Luo, R. Lin, J. Xu, Y. Hou, H. J. Snaith, H. Tan, *Science* **2022**, *376*, 762.

[2] L. Li, Y. Wang, X. Wang, R. Lin, X. Luo, Z. Liu, K. Zhou, S. Xiong, Q. Bao, G. Chen, Y. Tian, Y. Deng, K. Xiao, J. Wu, M. I. Saidaminov, H. Lin, C.-Q. Ma, Z. Zhao, Y. Wu, L. Zhang, H. Tan, *Nat. Energy* **2022**, *7*, 708.

[3] J. J. Yoo, G. Seo, M. R. Chua, T. G. Park, Y. Lu, F. Rotermund, Y.-K. Kim, C. S. Moon, N. J. Jeon, J.-P. Correa-Baena, V. Bulović, S. S. Shin, M. G. Bawendi, J. Seo, *Nature* **2021**, *590*, 587.

[4] Q. Jiang, L. Zhang, H. Wang, X. Yang, J. Meng, H. Liu, Z. Yin, J. Wu, X. Zhang, J. You, *Nat. Energy* **2016**, *2*, 16177.

[5] a) D. Yang, X. Zhou, R. Yang, Z. Yang, W. Yu, X. Wang, C. Li, S. Liu, R. P. H. Chang, *Energy Environ. Sci.* **2016**, *9*, 3071; b) S. S. Shin, E. J. Yeom, W. S. Yang, S. Hur, M. G. Kim, J. Im, J. Seo, J. H. Noh, S. I. Seok, *Science* **2017**, *356*, 167; ❑) H. Min, D. Y. Lee, J. Kim, G. Kim, K. S. Lee, J. Kim, M. J. Paik, Y. K. Kim, K. S. Kim, M. G. Kim, T. J. Shin, S. Il Seok, *Nature* **2021**, 598, 444; d) P. Zhang, J. Wu, T. Zhang,

Y. Wang, D. Liu, H. Chen, L. Ji, C. Liu, W. Ahmad, Z. D. Chen, S. Li, *Adv. Mater.* **2018**, *30*, 1703737.

[6] Q. Huaulmé, V. M. Mwalukuku, D. Joly, J. Liotier, Y. Kervella, P. Maldivi, S. Narbey, F. Oswald, A. J. Riquelme, J. A. Anta, R. Demadrille, Nature Energy 2020, 5, 468.

[7] M. M. Byranvand, T. Kim, S. Song, G. Kang, S. U. Ryu, T. Park, *Adv. Energy Mater.* **2018**, *8*, 1702235.

[8] H. Huang, P. Cui, Y. Chen, L. Yan, X. Yue, S. Qu, X. Wang, S. Du, B. Liu, Q. Zhang, Z. Lan, Y. Yang, J. Ji, X. Zhao, Y. Li, X. Wang, X. Ding, M. Li, *Joule* **2022**, *6*, 2186.

[9] W. Hu, W. Zhou, X. Lei, P. Zhou, M. Zhang, T. Chen, H. Zeng, J. Zhu, S. Dai, S. Yang, S. Yang, *Adv. Mater.* **2019**, *31*, 1806095.

[10] D. Yang, R. Yang, K. Wang, C. Wu, X. Zhu, J. Feng, X. Ren, G. Fang, S. Priya, S. Liu, *Nat. Commun.* **2018**, *9*, 3239.

[11] J. Peng, F. Kremer, D. Walter, Y. Wu, Y. Ji, J. Xiang, W. Liu, T. Duong, H. Shen, T. Lu, F. Brink, D. Zhong, L. Li, O. Lee Cheong Lem, Y. Liu, K. J. Weber, T. P. White, K. R. Catchpole, *Nature* **2022**, *601*, 573.

[12] Y. Ding, B. Ding, H. Kanda, O. J. Usiobo, T. Gallet, Z. Yang, Y. Liu, H. Huang, J. Sheng, C. Liu, Y. Yang, V. I. E. Queloz, X. Zhang, J.-N. Audinot, A. Redinger, W. Dang, E. Mosconic, W. Luo, F. De Angelis, M. Wang, P. Dörflinger, M. Armer, V. Schmid, R. Wang, K. G. Brooks, J. Wu, V. Dyakonov, G. Yang, S. Dai, P. J. Dyson, M. K. Nazeeruddin, Nat. *Nanotechnol.* **2022**, *17*, 598.

[13] P. Docampo, S. Guldin, U. Steiner, H. Snaith, *J. Phys. Chem. Lett.* **2013**, *4*, 698.

[14] M. Gopal, W. J. Moberly Chan, L. C. De Jonghe, *J. Mater. Sci.* **1997**, *32*, 6001.

[15] X. Wang, S. Shen, Z. Feng, C. Li, *Chinese J. Catal.* **2016**, *37*, 2059.

[16] J. Zheng, Z. Lei, *Appl. Catal. B* **2018**, *237*, 1.

[17] R. Azmi, C.-L. Lee, I. H. Jung, S.-Y. Jang, *Adv. Energy Mater.* **2018**, *8*, 1702934.

[18] W. Zhou, P. Zhou, X. Lei, Z. Fang, M. Zhang, Q. Liu, T. Chen, H. Zeng, L. Ding, J. Zhu, S. Dai, S. Yang, *ACS Appl. Mater. Interfaces* **2018**, *10*, 1897.

[19] P. Qin, T. Wu, Z. Wang, L. Xiao, L. Ma, F. Ye, L. Xiong, X. Chen, H. Li, X. Yu, G. Fang, *Adv. Funct. Mater.* **2020**, *30*, 1908408.

[20] L. Liu, S. Huang, Y. Lu, P. Liu, Y. Zhao, C. Shi, S. Zhang, J. Wu, H. Zhong, M. Sui, H. Zhou, H. Jin, Y. Li, Q. Chen, *Adv. Mater.* **2018**, *30*, 1800544.

[21] X. Gong, L. Guan, Q. Li, Y. Li, T. Zhang, H. Pan, Q. Sun, Y. Shen, C. Grätzel, S. M. Zakeeruddin, M. Grätzel, M. Wang, *Sci. Adv.* **2020**, *6*, eaay5661.

[22] T. Bu, J. Li, F. Zheng, W. Chen, X. Wen, Z. Ku, Y. Peng, J. Zhong, C. Bing, F. Huang, *Nat. Commun.* **2018**, *9*, 4609.

[23] S. Zhang, H. Si, W. Fan, M. Shi, M. Li, C. Xu, Z. Zhang, Q. Liao, A. Sattar, Z. Kang, Y. Zhang, *Angew. Chem. Int. Ed.* **2020**, *59*, 11573.

[24] K. Choi, J. Lee, H. I. Kim, C. W. Park, G.-W. Kim, H. Choi, S. Park, S. A. Park, T. Park, *Energy Environ. Sci.* **2018**, *11*, 3238.

[25] W. S. Yang, B.-W. Park, E. H. Jung, N. J. Jeon, Y. C. Kim, D. U. Lee, S. S. Shin, J. Seo, E. K. Kim, J. H. Noh, S. I. Seok, *Science* **2017**, *356*, 1376.

[26] F. Tan, H. Tan, M. I. Saidaminov, M. Wei, M. Liu, A. Mei, P. Li, B. Zhang, C.-S. Tan, X. Gong, Y. Zhao, A. R. Kirmani, Z. Huang, J. Z. Fan, R. Quintero-Bermudez, J. Kim, Y. Zhao, O. Voznyy, Y. Gao, F. Zhang, L. J. Richter, Z.-H. Lu, W. Zhang, E. H. Sargent, *Adv. Mater.* **2019**, *31*, 1807435.

[27] H. Yu, W. Zhao, L. Ren, H. Wang, P. Guo, X. Yang, Q. Ye, D. Shchukin, Y. Du, S. Dou, H. Wang, *Adv. Mater.* **2020**, *32*, 2070253.

[28] W. Zhao, P. Guo, J. Su, Z. Fang, N. Jia, C. Liu, L. Ye, Q. Ye, J. Chang, H. Wang, *Adv. Funct. Mater.* **2022**, *32*, 2200534.

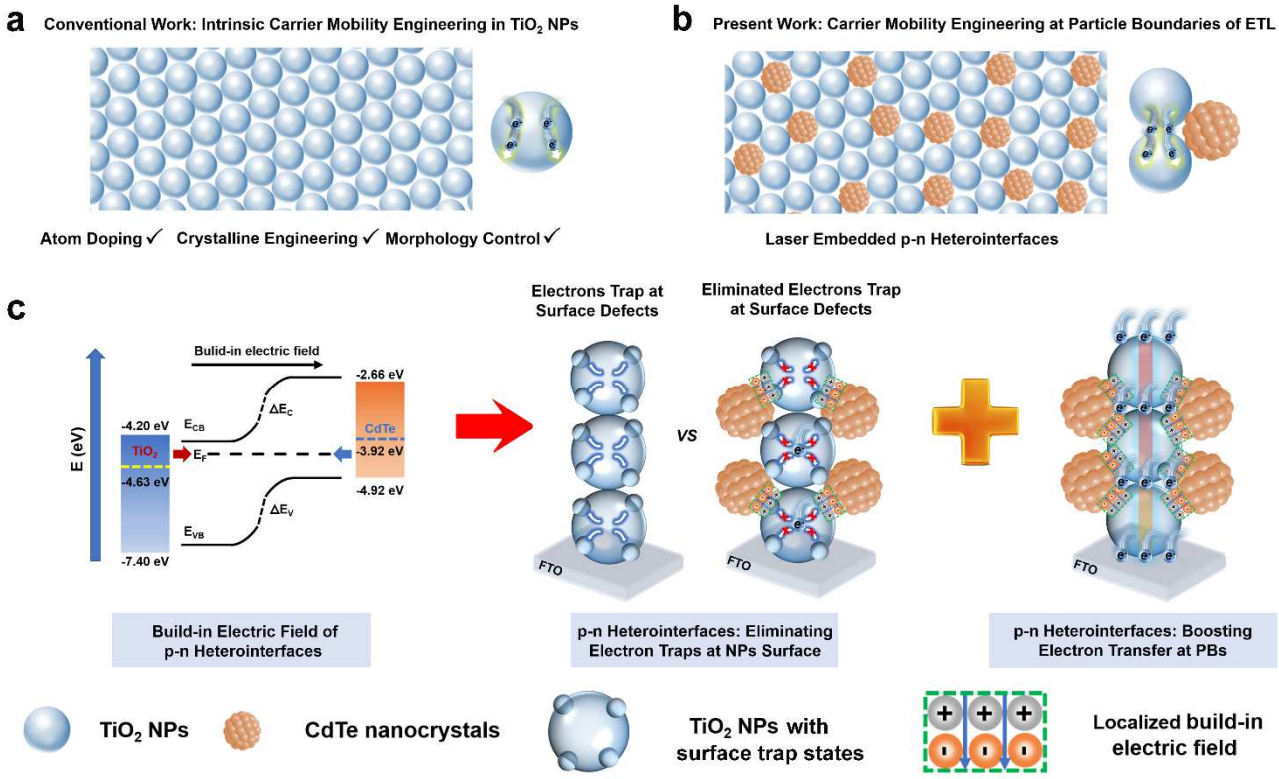

Scheme 1. (a) Schematic illustration of conventional work for the intrinsic carriers mobility of TiO_2 nanoparticles (NPs) based the electrons trapping at TiO_2 NPs. (b) Schematic illustration of present work for the particle boundaries (PBs) engineering of TiO_2 ETL. (c) Schematic illustration of the functions of embedded p-n heterointerfaces.

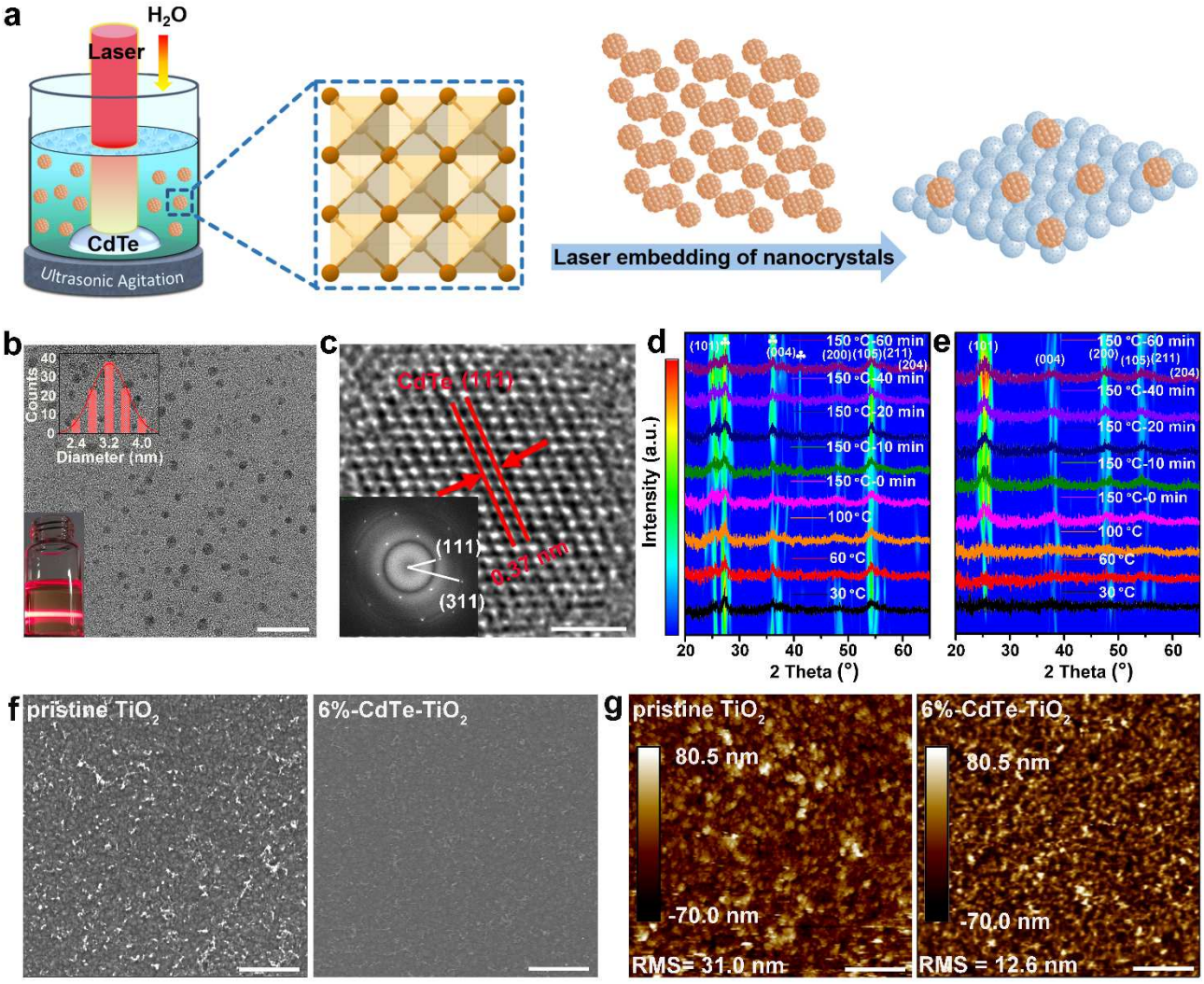

Figure 1. (a) Schematic illustration of the laser process of CdTe nanocrystals and its embedding in TiO_2 ETL matrix. (b) TEM image of CdTe nanocrystals (inset: nanocrystals size distribution diagram and Mie-scattering image of colloids loading CdTe nanocrystals via laser process). (c) HRTEM and corresponding FFT of CdTe nanocrystals. In-situ xrd patterns of TiO_2 with (e) and without (d) CdTe nanocrystals (♣: rutile phase). SEM (f) and AFM (g) images of pristine TiO_2 and 6%-CdTe-TiO_2 based ETLs. Scale bar: (b) 20 nm, (c) 2 nm, (f) 1 μm, (g) 1 μm.

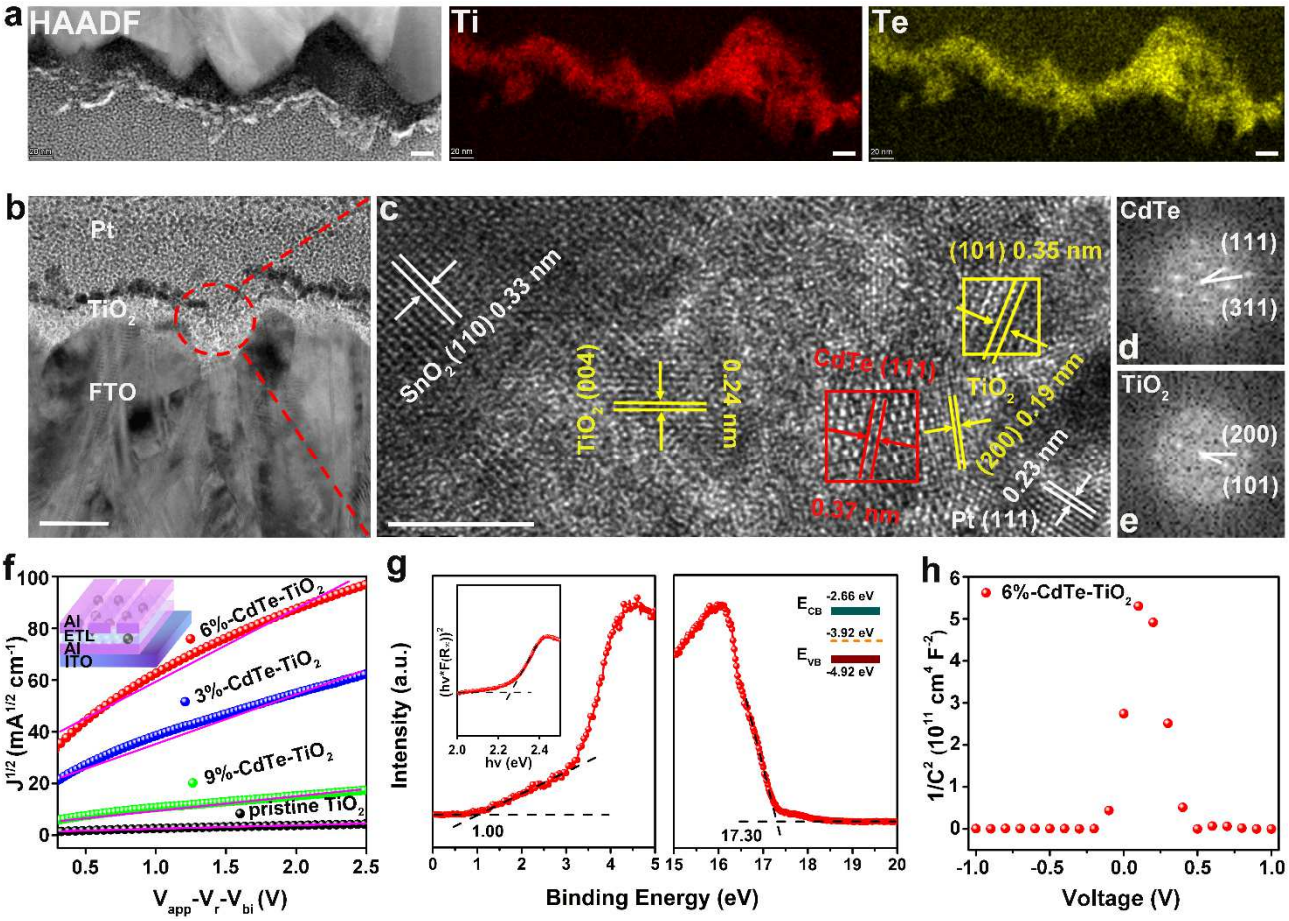

Figure 2. (a) Cross-sectional HAADF and corresponding TEM-EDS image of TiO_2 film with CdTe nanocrystals embedding. (b) Cross-sectional TEM and (c) HRTEM (magnified red region) conducted on the glass/FTO/CdTe-TiO2/Pt probing the existence of CdTe nanocrystals in the TiO_2 film. FFT-transformation images for CdTe nanocrystals (d: labeled as red area) and TiO_2 nanocrystals (e: labeled as yellow area). (f) Electron mobilities of different ETLs using the SCLC model, and the inset shows the device structure of ITO/Al/ETLs/Al. (g) UPS results of CdTe nanocrystals. (h) Mott-Schottky plots of CdTe nanocrystals embedded TiO_2 matrix. Scale bar: (a) 20 nm, (b) 50 nm, (c) 5 nm.

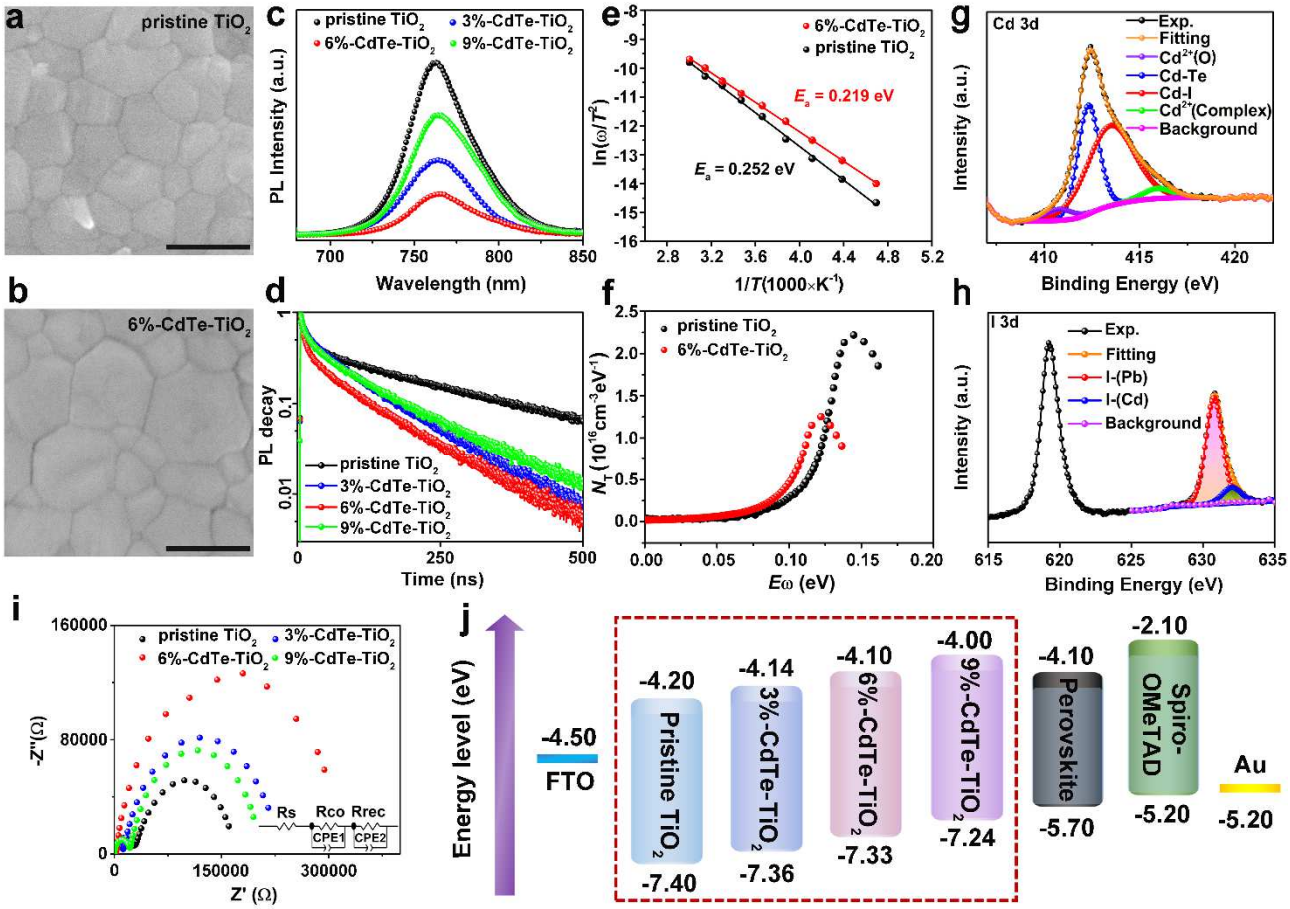

Figure 3. SEM images of perovskite films based pristine TiO_2 (a) and 6%-CdTe-TiO_2 films (b). (c) Steady-state and (d) time-resolved PL spectra of CsFAMA perovskite films spin-coated on different TiO_2 layers. (e) Arrhenius plots of the characteristic transition frequencies extracted from the derivative of the admittance spectra. (f) Trap state density (N_T) of the perovskite solar devices was measured at 300 K. High-resolution XPS spectra of Cd $3d_{3/2}$ (g) and I $3d_{3/2}$ (h) for CdTe nanocrystals-PbI_2 powder. (i) Nyquist curves of the devices upon different TiO_2 films measured in the dark at a bias of 0.8 V. Inset: the equivalent circuit model. (j) Energy level diagram for each component of devices upon different TiO_2 layers. The energy levels of Spiro-OMeTAD and Au refer to the literatures.[28] Scale bar: (a) 500 nm; (b) 500 nm.

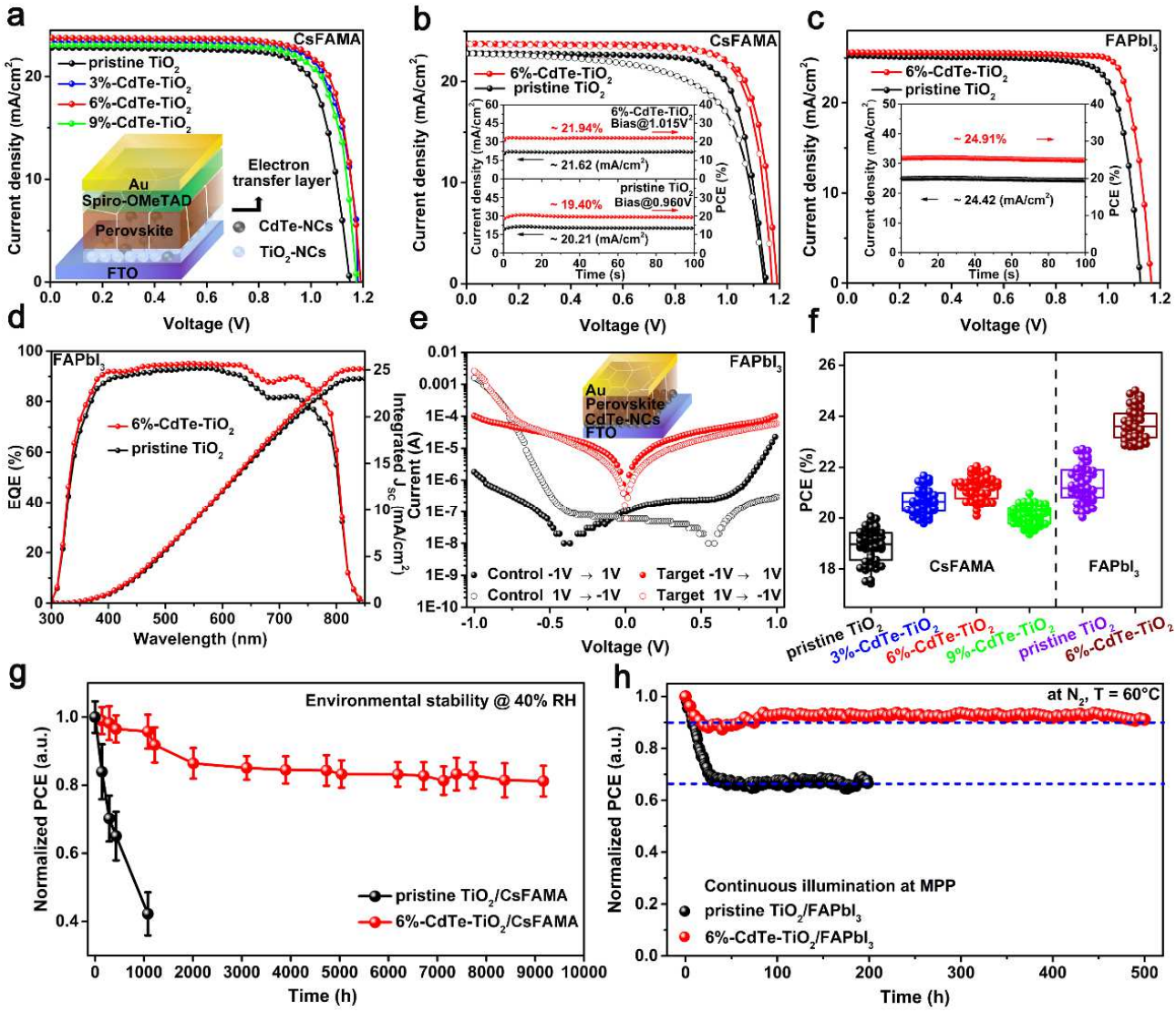

Figure 4. (a) *J-V* curves of the devices based on different TiO_2 layers with schematic illustration of device architecture. (b) *J-V* plots of the champion devices upon the pristine TiO_2 and 6%-CdTe-TiO_2 layers measured both in reverse scan and forward scan. Inset: the stabilized photocurrent and power output of champion devices at MPP. (c) *J-V* curves of $FAPbI_3$ devices based on different TiO_2 layers with stabilized photocurrent and power output. (d) The EQE spectra and the integrated current density for different champion devices. (e) The logarithmic *I-V* plots of different devices based the pristine TiO_2 and 6%-CdTe-TiO_2 layers, respectively. (f) PCE distribution of 50 individual CsFAMA and $FAPbI_3$ devices. The long-term humidity of CsFAMA-based devices (g), and operational (h) stability of $FAPbI_3$ devices with and without CdTe nanocrystals embedding. The error bars represent the standard deviation for 20 devices.

Table 1. Photovoltaic parameters of CsFAMA and $FAPbI_3$ type PSCs upon different TiO_2 ETLs.

Samples	Content of CdTe	*Voc* (V)	*Jsc* (mA/cm^2)	FF (%)	PCE (%)	
					Average	Best
Pristine TiO_2	0%	1.107±0.024	22.72±0.58	75.80±2.01	18.95±0.73	20.05
3%-CdTe-TiO_2	3%	1.155±0.020	23.38±0.33	76.60±1.48	20.66±0.63	21.68
6%-CdTe-TiO_2	6%	1.162±0.018	23.54±0.30	78.10±1.15	21.23±0.49	22.00
9%-CdTe-TiO_2	9%	1.141±0.022	22.98±0.47	75.97±1.64	20.15±0.70	20.98
Pristine $FAPbI_3$	0%	1.081±0.032	24.81±0.79	78.01±2.28	21.36±1.29	22.72
Target $FAPbI_3$	6%	1.131±0.026	25.41±0.60	80.21±1.78	23.81±0.85	25.05

Entry for the Table of Contents

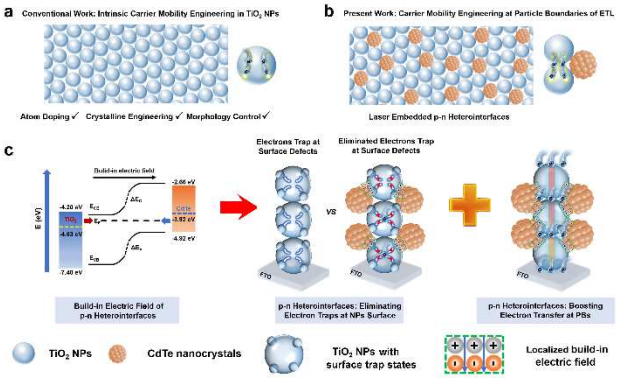

Present work demonstrates an efficient strategy of the particle boundaries (PBs) embedding of multifunctional p-type semiconducting CdTe nanocrystals for inhibited carrier losses at PBs, which could serve as efficient PBs mediator for boosting the electrons mobility of TiO_2 ETL by maximally three orders of magnitude and consequently result in a new benchmark PCE over 25% in planar PSCs.

Supporting Information

Laser Derived Electron Transport Layers with Embedded p-n Heterointerfaces Enabling Planar Perovskite Solar Cells with Efficiency over 25%

Wenhao Zhao[#], Pengfei Guo[#], Chen Liu, Ning Jia, Zhiyu Fang, Linfeng Ye, Qian Ye, Yadong Xu, Aleksandr P. Glotov, Andrei A. Novikov, Vladimir A. Vinokurov, Dmitry Shchukin and Hongqiang Wang[*]

W. Zhao, Dr. P. Guo, C. Liu, N. Jia, Z. Fang, L. Ye, Dr. Q. Ye, Prof. Y. Xu, Prof. H. Wang
State Key Laboratory of Solidification Processing, Center for Nano Energy Materials, School of Materials Science and Engineering, Northwestern Polytechnical University and Shaanxi Joint Laboratory of Graphene (NPU), Xi'an, 710072, P. R. China
Dr. P. Guo, Prof. H. Wang
Chongqing Innovation Center of Northwestern Polytechnical University, Northwestern Polytechnical University, Chongqing, 401135, China
E-mail: hongqiang.wang@nwpu.edu.cn
Prof. Y. Xu,
Northwestern Polytech Univ, State Key Lab Solidificat Proc, MIIT Key Lab Radiat Detect Mat & Devices, Xian 710072, P. R. China
Dr. A. P. Glotov, Dr. A. A. Novikov, Prof. V. A. Vinokurov
Gubkin Russian State University of Oil and Gas, Gubkin University, 19991, Moscow, 65/1 Leninsky prospect, Russia
Prof. D. Shchukin
Stephenson Institute for Renewable Energy, University of Liverpool, Liverpool L69 7ZF, UK
[#] These authors contribute equally to this work.

Experimental Section

Materials

Unless stated otherwise, all materials were purchased from Xi'an Polymer Light Technology Corp without further purification. Fuorine-doped tin oxide (FTO) coated glass substrates with partial etching (~20Ω) were purchased from Opvtech. The CdTe and GaAs bulk materials and some solvents including dimethylformamide (DMF), dimethylsulfoxide (DMSO), chlorobenzene (CB) and acetonitrile (ACN) were purchased from Sigma-Aldrich.

Preparation of ligand-free nanocrystals in desired solvent

A certain amount of the bulk materials are transferred into a chamber with 10 ml deionized water, subsequently suffering from a non-focusing nanosecond pulsed laser irradiation (Quantel, repetition rate: 10 Hz, pulse width: 8 ns, beam diameter: 8 mm) with a wavelength of 1064 nm. During the irradiation, continuous ultrasonic treatment is performed to ensure the preparation of homogeneous and well-dispersed CdTe colloids. The tailored laser fluence is applied ranging from 0-600 mJ/pulse cm^2.

Device Fabrication

Preparation of compact ETLs

The etched FTO substrates were cleaned sequentially in detergent, deionized water, acetone, isopropyl alcohol and ethanol under continuous sonication, and then dried with N_2 flow using a compressed nitrogen gun. After removing organic residues on the FTO substrates and improving wettability using an ozone plasma for 10 min, approximately 50 nm thick TiO_2 compact layer prepared by chemical bath deposition is deposited on clean FTO substrate immersed in a $TiCl_4$ aqueous solution (2.25:100 volume ratio of $TiCl_4$: H_2O) at 70 °C for 1 h, and then annealed at 150 °C for 60 min.

For the target ETLs configuration, $TiCl_4$ precursor incorporating different content of CTNs with 0.1mg/ml concentration (3%, 6% and 9% volume ratio to $TiCl_4$ precursor abbreviated as 3%-CdTe-TiO_2, 6%-CdTe-TiO_2, 9%-CdTe-TiO_2) and then together with FTO substrates are subject to similar thermal processing.

Fabrication of perovskite films

CsFAMA-based perovskite: The spin-coating procedure was carried out in a nitrogen glove box. For the fabrication of $Cs_{0.05}FA_{0.81}MA_{0.14}PbI_{2.57}Br_{0.43}$ perovskite, the precursor solution (1.25 M) containing CsI (0.0625M), FAI (1.0125 M), PbI_2 (1.075 M), MABr (0.175M) and $PbBr_2$ (0.175M) is prepared with a successive stir in a mixture of DMF: DMSO (4:1 v/v) at 55 °C for 2 h. The as-prepared precursor (30 μL) was dropped onto the TiO_2/FTO substrate followed by a consecutive two-step spin-coating process at 2,000 and 4,000 rpm for 10 and 30 s, respectively. During the second spin-coating step, 200 μL anhydrous chlorobenzene (CB) was immediately poured on the substrate 10 s prior to the end of the program. Afterwards, the intermediate phase film is heat-treated on a hotplate at 100 °C for 60 min.

$FAPbI_3$-based perovskite: The perovskite precursor (1.80M) containing FAI (1.80M), PbI_2 (1.80M)，FAHCOO (0.12M) and MACl (0.52M) is prepared with a successive stir in a mixture of DMF: DMSO (4:1 v/v) at 55 °C for 2 h. The as-prepared precursor (30 μL) was dropped onto the TiO_2/FTO substrate followed by a one-step spin-coating at 6000 rpm for 50 s. During spin coating, 200 μL chlorobenzene (CB) is immediately poured on the substrate 15 s prior to the end of the program. Subsequently, the intermediate phase film is heat-treated on a hotplate at 150 °C for 10 min.

In addition, for $FAPbI_3$ type perovskite, 3mg/ml phenethylammonium iodide (PEAI) was spin-coated on the perovskite/TiO_2/FTO substrate at 6000 rpm for 30 s, followed by deposition of Spiro-OMeTAD.

The deposition of HTM and Au electrode

The hole-transport layer was deposited onto the perovskite/TiO_2/FTO substrate via spin-coating at 6000 rpm for 30 s, prepared by dissolving 72.3 mg Spiro-OMeTAD, 29 mL tBP and 18 μL Li-TFSI (a stock solution of 520 mg/mL in acetonitrile) into 1 mL chlorobenzene. Finally, the Au electrode (80 nm) was deposited on the top of devices by thermal evaporation using a shadow mask. Each electrode of devices exhibits the active area of 0.05 cm^2, and during testing, that of each electrode is accurately defined by a 0.045 cm^2 non-reflective mask to eliminate the influence of any edge effects.

Characterization

The SEM images and relevant EDS results were obtained by using a field emission SEM with an EDS detector (FEI Nova). Atomic force microscope (AFM) characterization was performed using a Bruker Dimension Icon. High-resolution transmission electron microscopy (HRTEM) with EDS were characterized employing an FEI Tecnai F30 transmission electron microscope operated at 300 kV, equipped with an Oxford Instruments EDS

detector and a high angle annular dark field (HAADF) STEM detector. The cross sections of TiO_2 films are prepared by focused ion beam (FIB). The Raman spectra was acquired using a Raman microscope at an excitation laser wavelength of 532 nm (Renishaw). The X-ray diffraction (XRD) patterns were characterized on a X'pert PRO (PANalytical) using a Cu Kα (λ = 0.15406 nm) as the X-ray source. The absorption plots were acquired using the ultraviolet-visible (UV-vis) spectrophotometer (Perkin-Elmer Lambda 35 UV-vis-NIR). The steady-state photoluminescence and time-resolved photoluminescence (TRPL) spectra were measured using pulse laser excitation source at the wavelength of 470 nm (Horiba FluorologFL-3). The two-probe conductivity measurements were carried out on an electrochemical workstation (CHI660E) using linear sweep voltammetry at room temperature in the dark. The EIS was measured applying a bias of 0.8V in the dark in a frequency range from 1 MHz to 0.1 Hz (CHI660E). For Mott–Schottky analysis, capacitance–voltage measurements were performed at a frequency of 1 kHz with devices configuration of FTO/ETLs/Perovskite/Au without a hole-transport layer (CHI660E). X-ray photoelectron spectroscopy (XPS) measurements were conducted on an Axis Supra (Kratos). Ultraviolet photoelectron spectroscopy (UPS) was characterized by a VG Scienta R4000 analyzer and the HeI (21.22eV) emission line employed for excitation at a bias of -5V. The contact angles measurements were performed on a Data physics OCA-20 contact-angle system at ambient air. The J–V curves and maximum power point tracking were measured via a Keithley 2400 source meter under simulated AM 1.5G illumination (100 mW cm^{-2}) produced by a xenon-lamp-based solar simulator (Oriel 67005, 150 W Solar Simulator) that was calibrated with a monocrystalline silicon reference cell (Hamamatsu S1133). The devices were measured both in reverse scan (+1.2 V to -0.1 V) and forward scan (-0.1 V to +1.2 V) with a scanning rate of 0.2V/s. The EQE was obtained by using a Enlitech EQE measurement system (QE-R3011). The dark I-V characterization of the electron-only devices were measured by a Keithley 2400 source to calculate the trap state density using SCLC model.

Calculations

Calculations for included angle of CdTe crystal planes (cubic):

$$\cos\theta = \frac{h_1h_2 + k_1k_2 + l_1l_2}{\sqrt{({h_1}^2 + {k_1}^2 + {l_1}^2)\,({h_2}^2 + {k_2}^2 + {l_2}^2)}} \quad (1)$$

Calculations for included angle of TiO_2 crystal planes (tetragonal):

$$\cos\theta = \frac{\frac{h_1h_2 + k_1k_2}{a^2} + \frac{l_1l_2}{c^2}}{\sqrt{\left(\frac{h_1^{\,2} + k_1^{\,2}}{a^2} + \frac{l_1^{\,2}}{c^2}\right)\left(\frac{h_2^{\,2} + k_2^{\,2}}{a^2} + \frac{l_2^{\,2}}{c^2}\right)}} \quad (2)$$

where θ is the included angle of crystal planes; a, c are crystal lattice constants; h_1, k_1, l_1, h_2, k_2 and l_2 are specific crystal indices.

Calculation for the electron mobility (μ) of different ETLs using SCLC model:

$$\mu = \frac{8JL^3}{9\varepsilon\varepsilon_0(V - V_r - V_{bi})^2} \quad (3)$$

where J is the current density; L is the thickness of different TiO_2 films; ε_0 and ε are the vacuum permittivity and the dielectric permittivity, respectively. V is the applied voltage, V_r is the voltage loss resulting from radiative recombination, and V_{bi} is the built-in potential.[1]

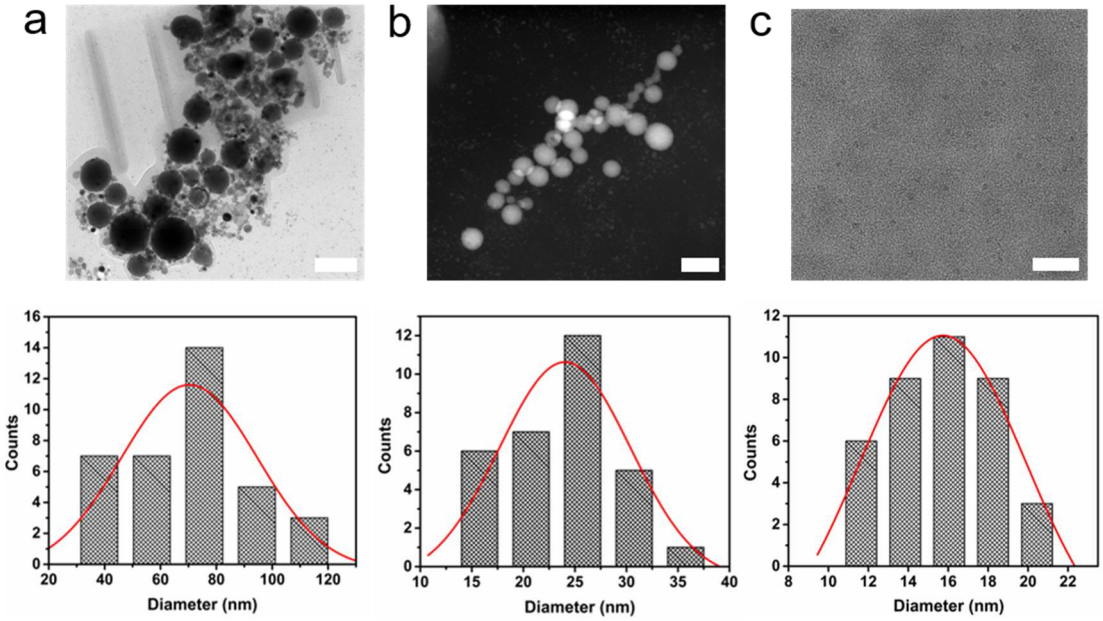

Figure S1. CdTe nanoparti□les with different size distribution via various laser fluen□e of 300, 400 and 500 mJ pulse^{-1} □m^{-2} produ□ing nanoparti□les with average size of approximately 73 nm, 25 nm and 17 nm, respe□tively. S□ale bars: (**a**) 100 nm, (**b**) 50 nm, (**c**) 100 nm.

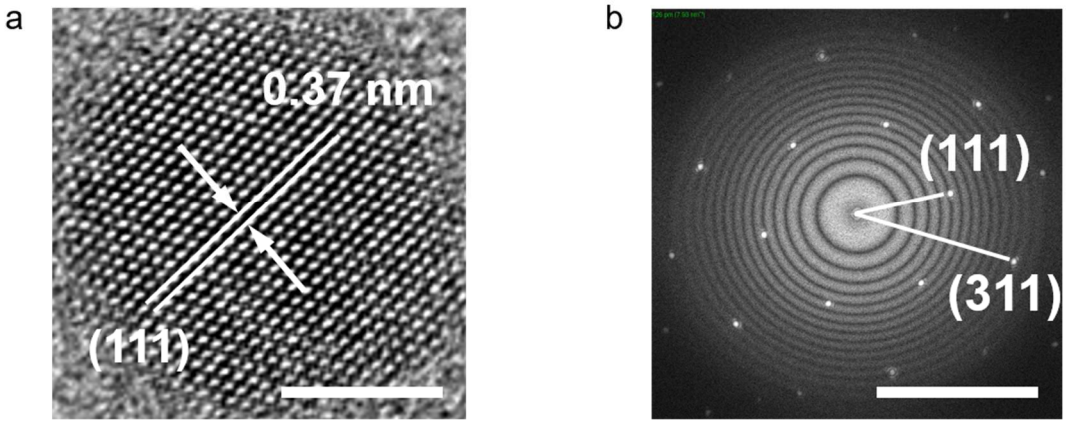

Figure S2. HRTEM (**a**) and □orresponding FFT-transformation (**b**) images for laser generated CdTe nanoparti□les, exhibiting the (111) and (220) plane with 35.3° plane in□luded angle. S□ale bars: (**a**) 5 nm, (**b**) 1/5 nm.

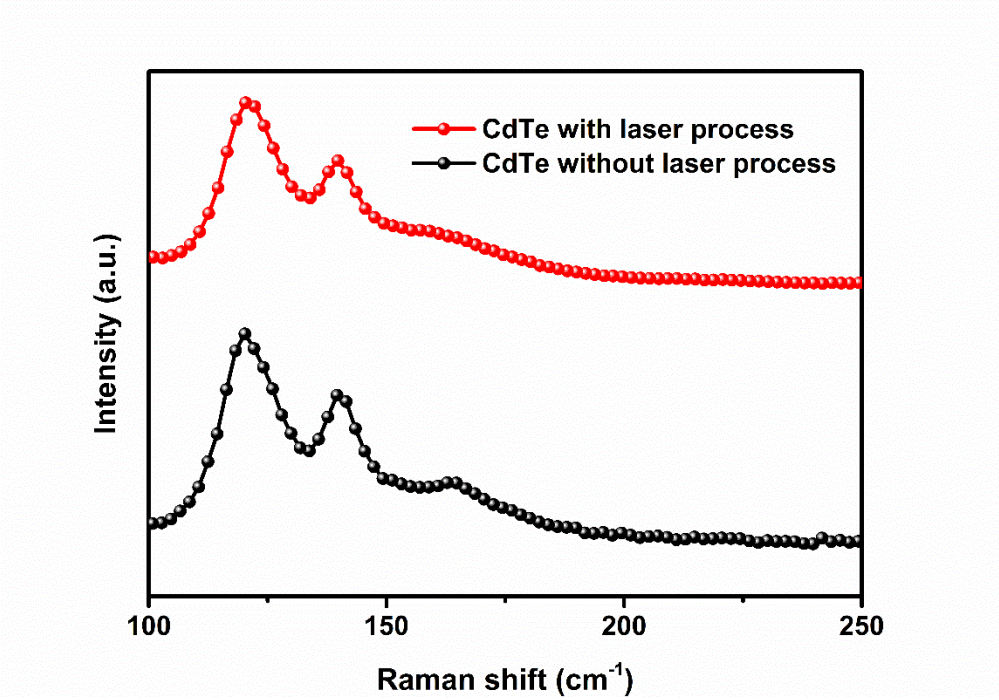

Figure S3. Raman spectroscopy of CdTe with and without laser irradiation process.

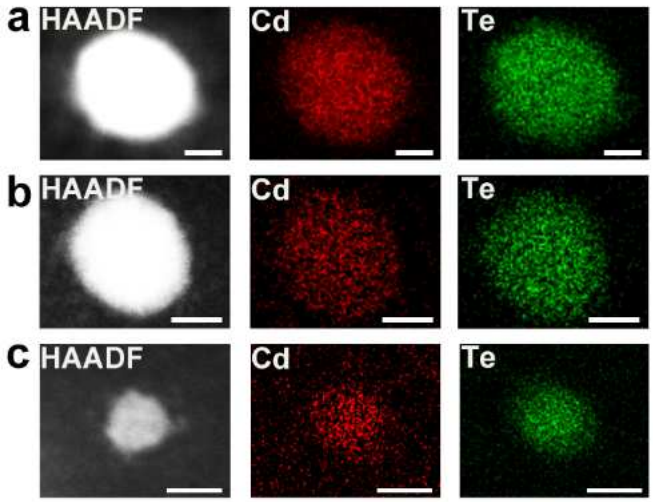

Figure S4. HAADF and corresponding TEM-EDS images of CdTe nanoparticles produced by pulsed laser process with different laser fluence. Scale bar: (a) 20 nm, (b) 10 nm, (c) 10 nm.

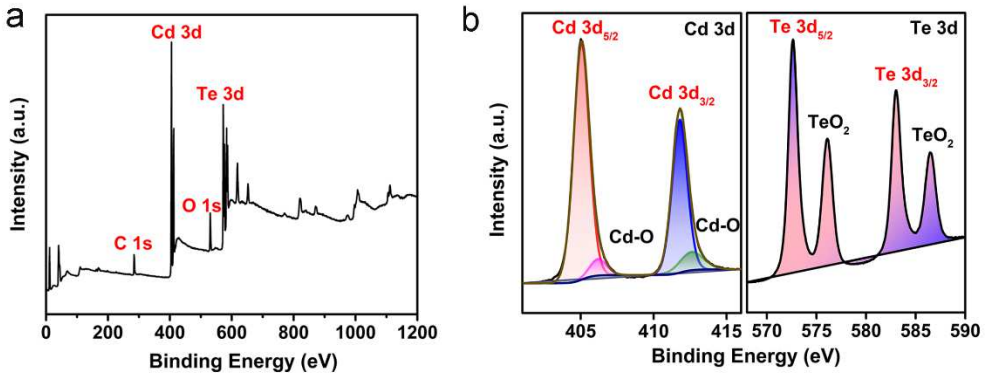

Figure S5. XPS spectrum (a) and high-resolution XPS spectra (b) of CdTe nanocrystals. The appearances of Cd $3d_{3/2}$ peak at 412.1 eV, Cd $3d_{5/2}$ peak at 405.1 eV, Te $3d_{5/2}$ peak at 572.8 eV, and Te $3d_{3/2}$ peak at 583.2 eV confirm the existence of cadmium and tellurium species in the CdTe nanocrystals.[2]

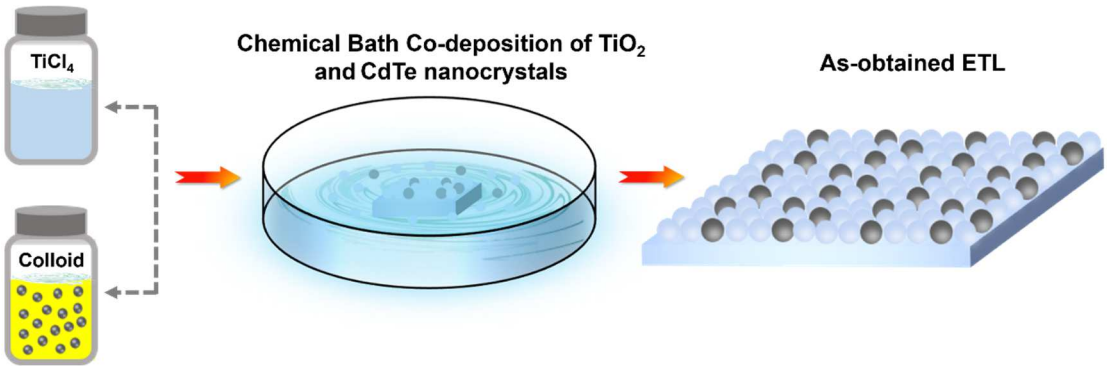

Figure S6. S□hemati□illustration of embedding of CdTe nano□rystals in the TiO_2 matrix.

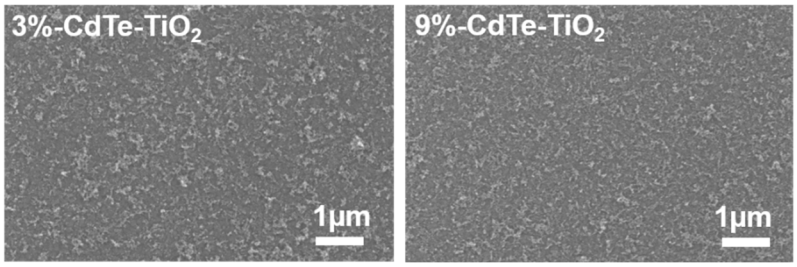

Figure S7. SEM top-view images of , 3%-CdTe-TiO_2 and 9%-CdTe-TiO_2 films.

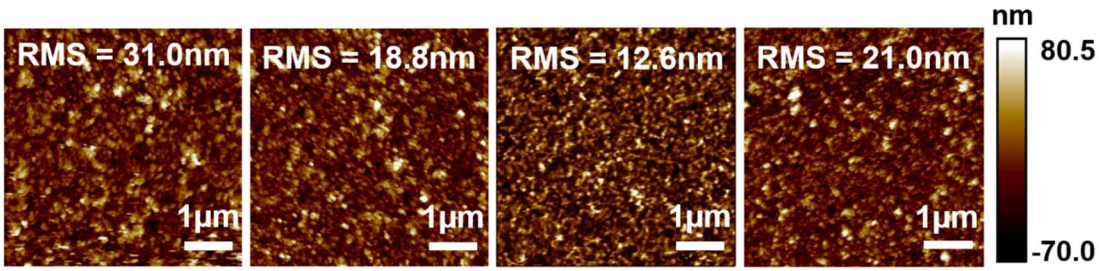

Figure S8. AFM height images of pristine TiO_2, 3%-CdTe-TiO_2, 6%-CdTe-TiO_2 and 9%-CdTe-TiO_2 films.

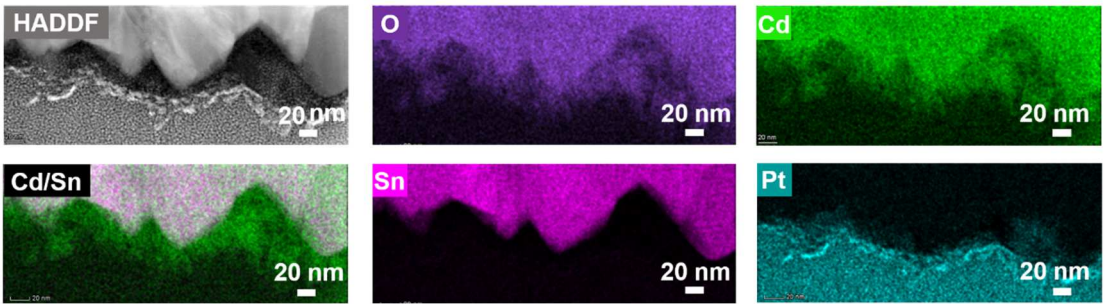

Figure S9. TEM-EDS mapping of cross-sectional TEM for Ti, O, Cd, Te, Cd/Sn, Sn, and Pt elements. Scale bars: 20 nm.

a

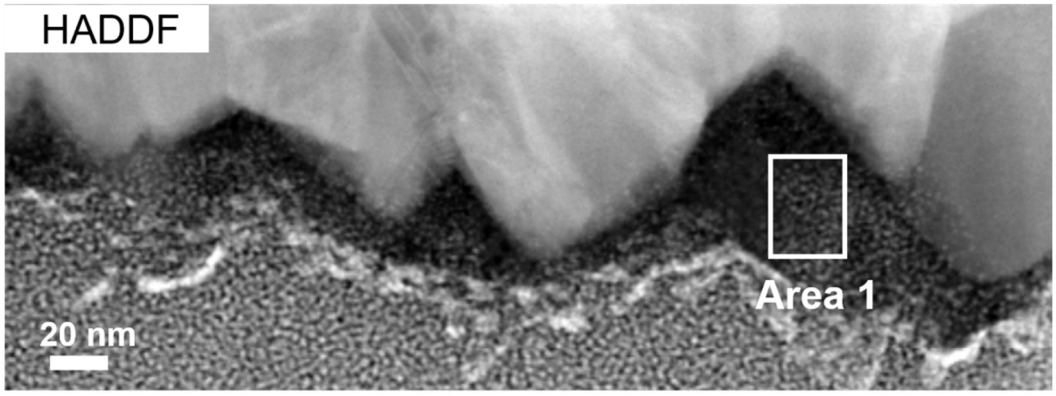

b

Elements	Family	Atomic Fraction (%)	Atomic Errors(%)	Mass Fraction (%)	Mass Error(%)
O	K	72.35	7.88	46.09	3.39
Ti	K	27.24	4.64	51.92	7.79
Cd	L	0.21	0.06	0.93	0.24
Te	L	0.21	0.05	1.06	0.26

c

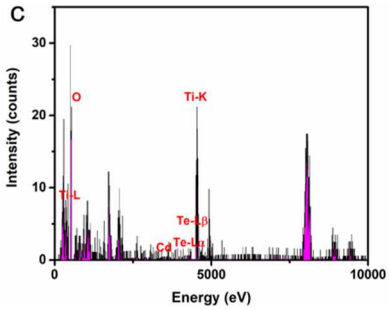

Figure S10. Cross-se□tional TEM-EDS results of 9%-CdTe-TiO_2 films with all elements □ontent analyses (**b**) from sele□ted area 1 of HADDF image (**a**) and □orresponding s□hemati□diagram (**c**).

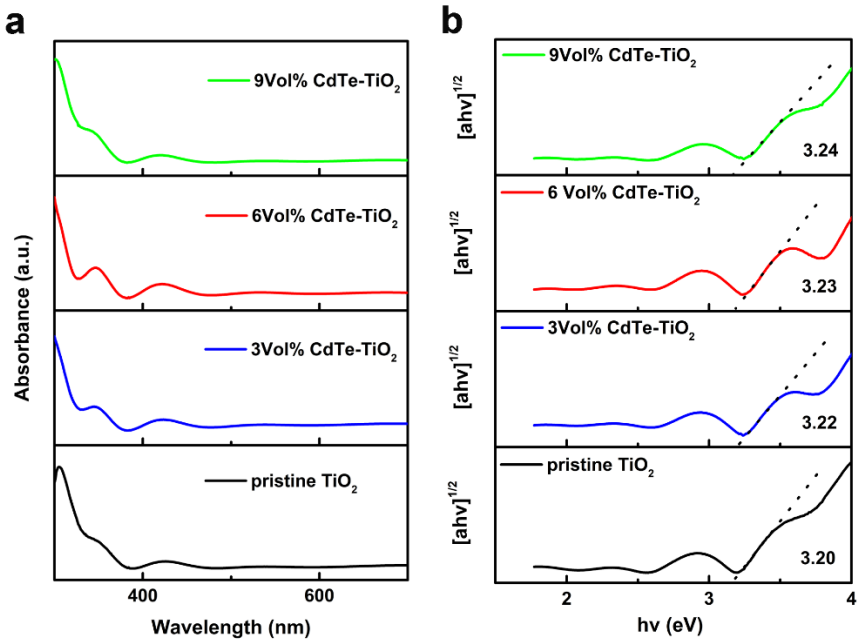

Figure S11. Absorption spectra (**a**) of different TiO_2 films and corresponding Tauc plots (**b**) determining the optical bandgaps of TiO_2 films.

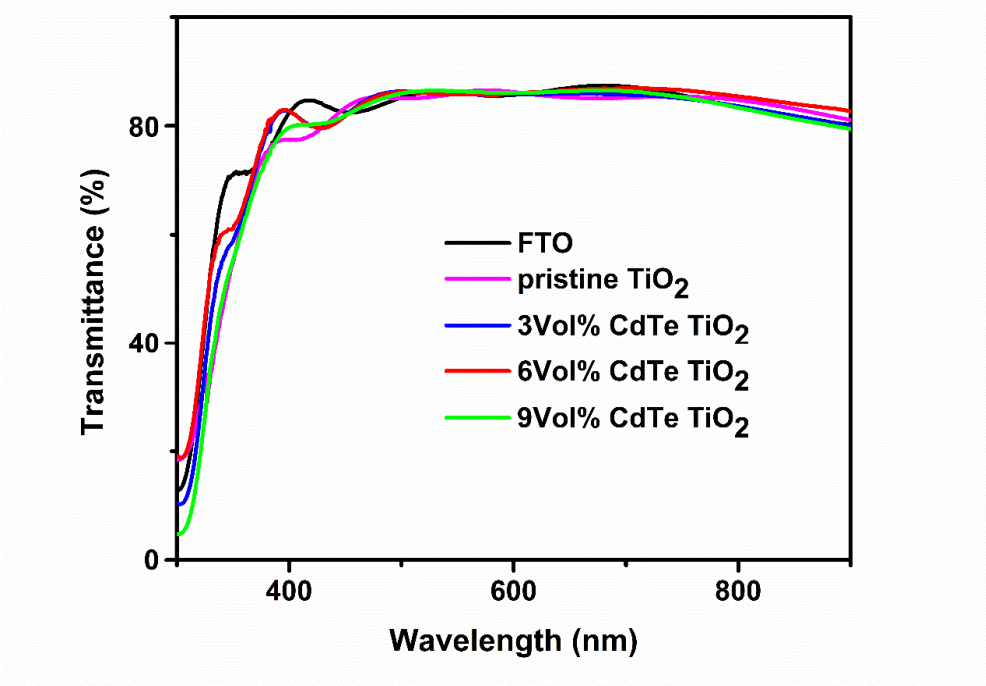

Figure S12. Optical transmittance spectra of FTO and different TiO_2 films based on FTO.

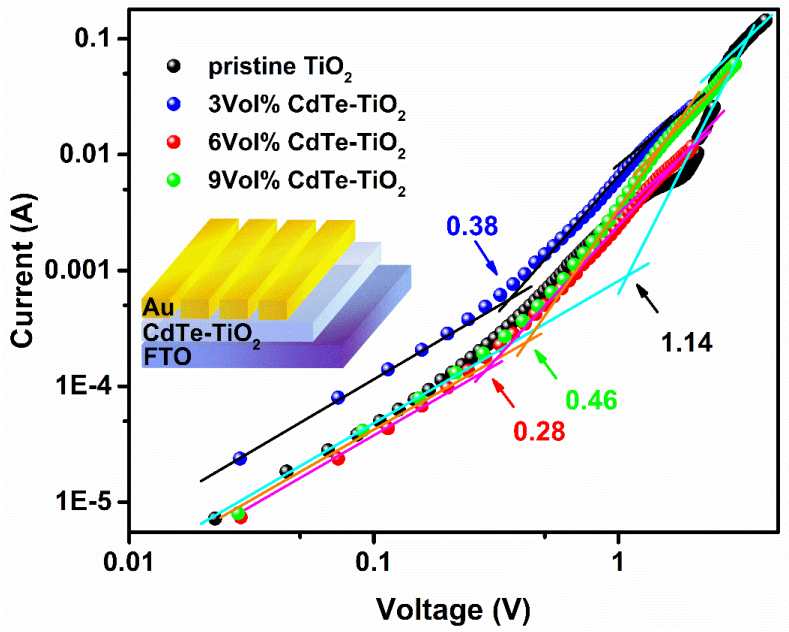

Figure S13. *I-V* curves with V_{TFL} related to the N_t of different ETLs and corresponding device structure of FTO/ETL/Au.

Table S1. The dark *I-V* plots of different devices show V_{TFL} (the onset voltage of the trap-filled limit region) kink point behavior, it could be extracted to determine the N_t of various ETLs. The N_t of different ETLs was evaluated using $N_t = \frac{2\varepsilon_0 \varepsilon V_{TFL}}{qL^2}$ formula, where ε_0 is the vacuum permittivity, ε is the relative dielectric constant, V_{TFL} is the onset voltage of the trap-filled limit region, q is the elemental charge, and L is the thickness of the ETLs.[3]

ETLs	V_{TFL} (V)	N_t (cm^{-3})
Control	1.14	3.95×10^{16}
3%-CdTe-TiO_2	0.38	1.32×10^{16}
6%-CdTe-TiO_2	0.28	9.70×10^{15}
9%-CdTe-TiO_2	0.46	1.59×10^{16}

Note S1: preparation of the TiO_2 films for the measurement of the electron mobilities

We estimate the electron mobilities of the TiO_2 films as reported in the literature[4] using the electron-only devices with a structure of ITO/Al/ETLs/Al. Detailly, Al (80 nm) is deposited on ITO substrates, and then TiO_2 powder prepared by drying TiO_2 aqueous solution with and without CdTe-NCs after suffering thermal treatment of 70 ℃ are dispersed in anhydrous ethanol (5 mg/ml) with the addition of titanium(diisopropoxide) bis(2,4-pentanedionate) (TIPD: 15 ul/ml),[5] then spin-coated on ITO substrates at 5000 rpm for 40s for twice, followed by annealing at 150℃ for 60 min. Finallly, Al (80 nm) is deposited on different samples by thermal evaporation.

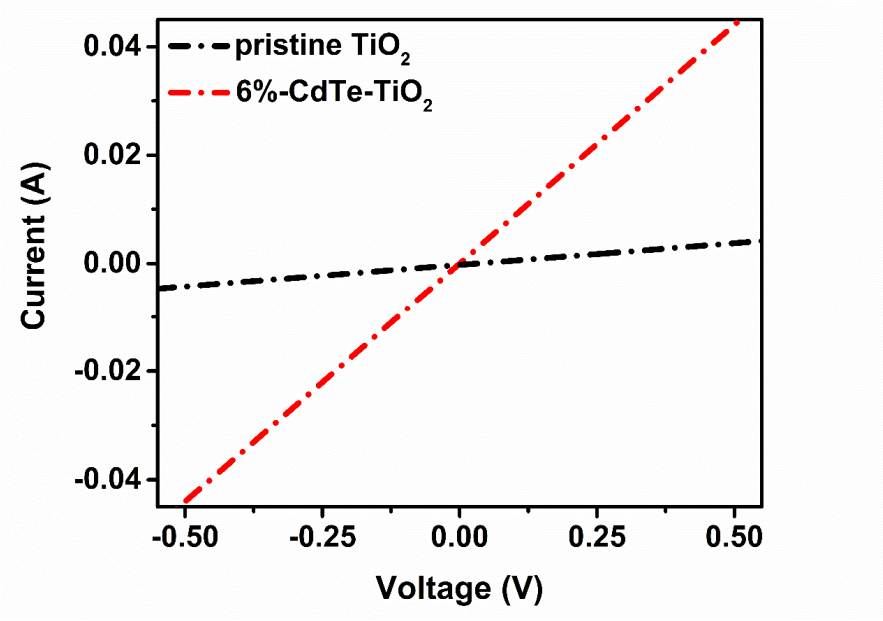

Figure S14. Conduction properties of pristine TiO_2 and 6%-CdTe-TiO_2 films measured by a device structure of FTO/ETL/Ag. The conductivity of different ETLs was evaluated using $\sigma = \frac{Id}{VA}$ formula, where A is the area of devices, d is the thickness of ETLs. The results indicate that CdTe embedded TiO_2 yields larger conductivity based larger slope.[6]

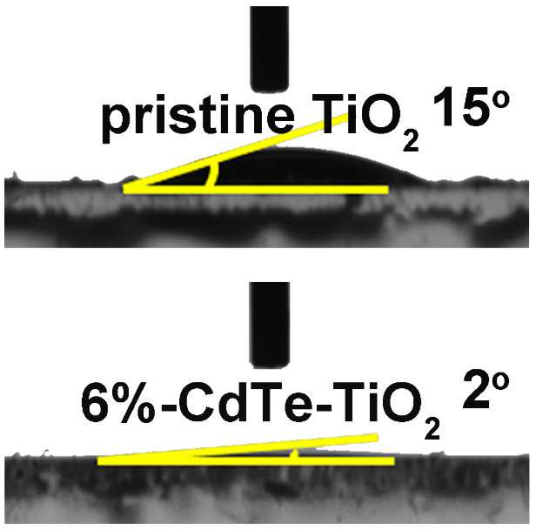

Figure S15. Contact angle of pristine TiO_2 and 6%-CdTe-TiO_2 films dropped by perovskite precursor.

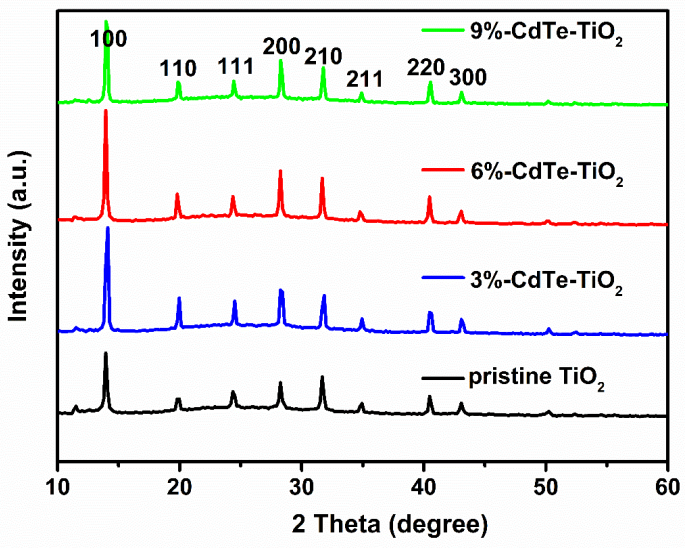

Figure S16. XRD pattern of perovskite films upon different TiO_2 layers.

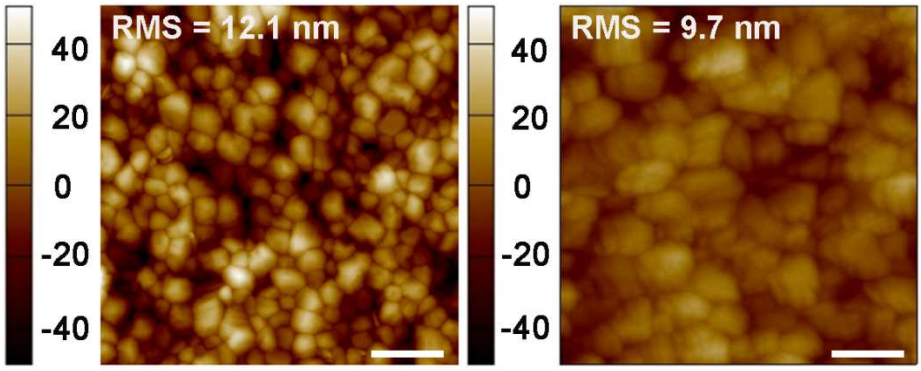

Figure S17. AFM images of perovskite films based pristine TiO_2 and 6%-CdTe-TiO_2 films.

Table S2. Summaries of parameters extracted from the fitted plots of the corresponding TRPL spectra following bi-exponential rate law: $f(t) = A_1\exp(-t/\tau_1) + A_2\exp(-t/\tau_2) + y_0$, where A_1 and A_2 represent the relative amplitudes, τ_1 represents trap-assisted recombination, and τ_2 represents free carrier recombination. The τ_{ave} is calculated using $\tau_{ave} = \frac{\sum A_i \tau i^2}{\sum A_i \tau i}$ formula.[7]

ETLs	A_1	τ_1 (ns)	A_2	τ_2 (ns)	τ_{ave} (ns)
Control	0.67	11.45	0.33	267.51	247.04
3 Vol%	0.58	9.27	0.42	102.91	92.55
6Vol%	0.78	6.44	0.22	99.51	82.14
9 Vol%	0.64	9.90	0.36	122.87	108.72

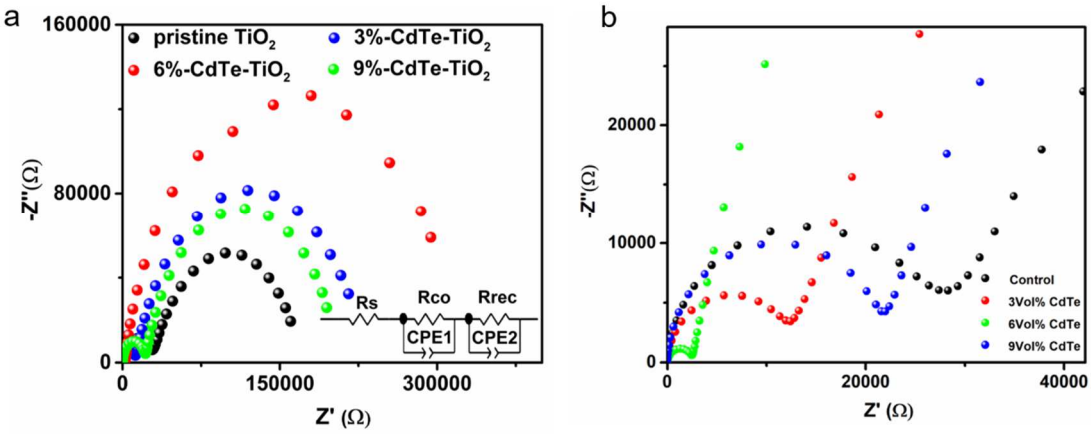

Figure S18. (a) Nyquist curves of the devices upon different TiO_2 films measured in the dark at a bias of 0.8 V. Inset: the equivalent circuit model. (b) The high-frequency regions of Nyquist plots of devices based on different ETLs. The Nyquist plots of devices upon different TiO_2 ETLs measured in the dark under a bias of 0.8 V exhibits two diagnostical characteristic arcs in high-frequency and low-frequency assigned to the contact resistance (R_{co}) and the recombination resistance (R_{rec}) of charge carriers, respectively. The corresponding insets represent the equivalent circuit model and relevant fitting parameters are detailly listed in Table S3.

Table S3. Summaries of parameters extracted from the fitted plots of the impedance spectra of devices upon differnent ETLs using a the equivalent circuit model.

ETLs	Rs (Ω)	Rco (Ω)	CPE1-T (F)	CPE1-P (F)	Rrec (Ω)	CPE2-T (F)	CPE2-P (F)
control	20.11	27159	6.20E-09	0.94	1.47E05	1.82E-06	0.76
3Vol%	9.86	11740	5.60E-09	0.97	2.21E05	1.11E-06	0.80
6Vol%	4.08	2422	6.30E-09	0.96	3.11E05	1.03E-06	0.87
9Vol%	11.39	20910	4.18E-09	0.99	1.85E05	1.14E-06	0.84

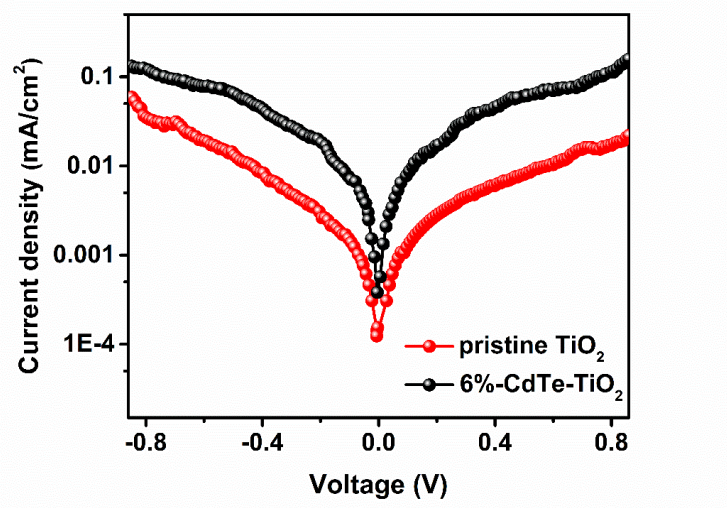

Figure S19. Dark current density-voltage plot of devices based the pristine TiO_2 and 6%-CdTe-TiO_2 films.

Note S2: the calculation of energy level of TiO_2 films with and without CdTe nanocrystals embedding

The Fermi level (E_F) is calculated using $E_F = E_{cut\text{-}off}$ - 21.22 eV equation, where $E_{cut\text{-}off}$ represents cut-off binding energy, 21.22 eV is the photon energy of excitation light. The $E_{cut\text{-}off}$ values are 16.59, 17.54, 17.58, and 17.62 eV for different TiO_2 layers. The calculated E_F values show -4.63, -3.68, -3.64 and -3.60 eV for the pristine TiO_2, 3%-CdTe-TiO_2, 6%-CdTe-TiO_2 and 9%-CdTe-TiO_2 layers, respectively. And then the valence band (E_{VB}) is calculated using $E_{VB} = E_F - E_F$, edge (Fermi edge) equation, obtaining -7.40, -7.36, -7.33 and -7.24 eV for different TiO_2 layers. The band gap (E_g) values of TiO_2 are extracted from the absorption spectrum and corresponding Tauc plot, revealing negligible change on E_g (3.20, 3.22, 3.23 and 3.24 eV for different TiO_2 layers). Then the calculated conduction bands (E_{CB}) reflected from E_g and E_{VB} are -4.20, -4.14, -4.10 and -4.00 eV for different TiO_2 layers, respectively.

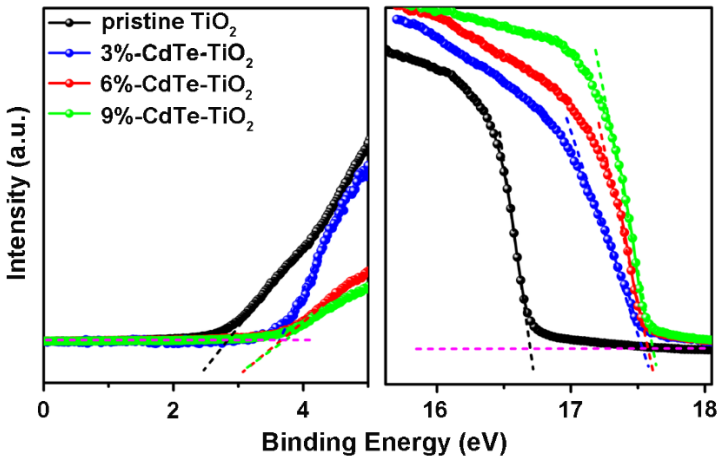

Figure S20. Different TiO_2 films with UPS Fermi edge (left) and the cut-off energy (right).

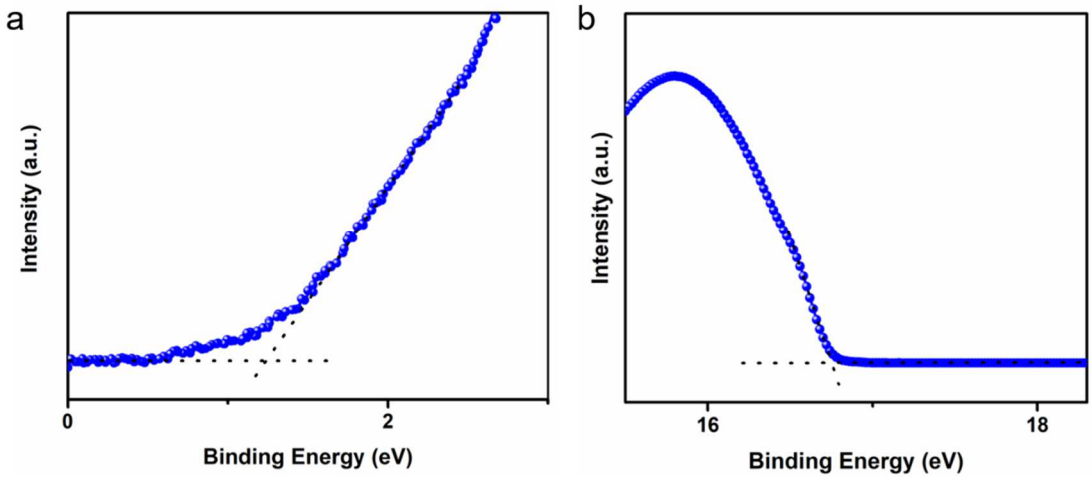

Figure S21. UPS Fermi edge (**a**) and the cut-off energy (**b**) of CsFAMA perovskite film.

Note S3: AS and Mott-Schottky analyses

By virtue of the limitations of the space charge-limited current (SCLC) for defect analysis, temperature dependent admittance spectroscopy (AS) along with Mott-Schottky analysis is widely employed to quantitatively characterize both shallow and deep defects in PSCs. As the previous literature reported,[8] the defect activation energies (E_a) is derived via the equation:

$$\omega_0 = \beta T^2 exp(\frac{-E_a}{K_b T})$$

where $\omega_0$is the characteristic transition angular frequency, β is a temperature dependent parameter, T is the temperature and $K_b$is the Boltzmann's constant, respectively. The derivative of the capacitance spectrum can be used to determine ω_0 from the peak value of the $[-\omega \times dC/d\omega]$ curve. According to this relation, the value of E_a can be obtained from the slope of the graph by fitting the Arrhenius formula[8]:

$$\ln\frac{\omega_0}{T^2} = \ln\beta - \frac{E_a}{K_b T}$$

the trap density (N_t) can be derived pursuant to the equation[8]:

$$N_t(E_\omega) = -\frac{V_{bi}}{qW}\frac{dC}{d\omega}\frac{\omega}{k_b T}\ , \quad E_\omega = K_b T \ln\frac{\beta T^2}{\omega}$$

where V_{bi} is the built-in potential, C is the capacitance, ω is the applied angular frequency, q is the elementary charge, and W is the depletion width, respectively. The values of V_{bi} and W were obtained from the Mott-Schottky analysis[8]:

$$\frac{A^2}{C^2} = \frac{2(V_{bi} - V)}{q\varepsilon\varepsilon_0 N}$$

where A is the active area, ε is the static permittivity of perovskite, ε_0 is the permittivity of free space, N is the apparent doping profile in the depleted layer, and V is the applied bias. The Mott-Schottky plot describes a straight line where the intersection on the bias axis determines V_{bi} and the slope gives the impurity doping density N. Then, the depletion width $W = \sqrt{\frac{2\varepsilon\varepsilon_0 V_{bi}}{qN}}$ corresponding to the zero bias can be calculated, the distribution of trap state density can be calculated. **Figure S22a-b** show the temperature-dependent AS of the devices based pristine TiO_2 and 6%-CdTe- TiO_2 ETLs measured at temperatures ranging from 210 to 330 K under the dark. The corresponding Arrhenius plots of these two devices describe the relationship between the characteristic transition frequencies and temperatures (**Figure 3e**). The calculated defect activation energies (E_a) of the control and target samples are 0.252 and 0.219 eV, respectively. The built-in potential (V_{bi}) and the depletion width (W) are determined from the Mott-Schottky analysis of the data measured at a frequency of 1 kHz with bias potential from 0 to 1.2 V (**Figure S22c**). After calculation, the V_{bi} of the control and target devices are 0.92 and 1.02 V, and the corresponding depletion widths are 185 and 290 nm, respectively. The density distribution and energy levels of trap states in these two devices are then presented in **Figure 3f**.

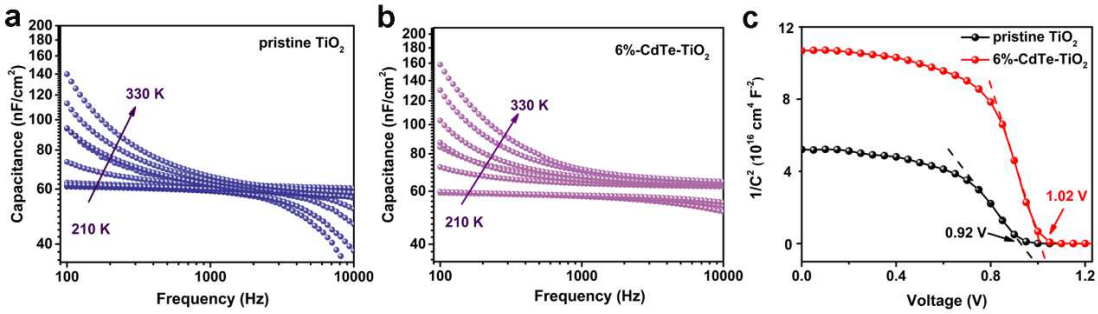

Figure S22. Admittance spectra of devices based on pristine TiO_2 (a) and 6%-CdTe- TiO_2 (b) ETLs, which were measured at gradient temperatures between 210 and 330 K with a step of 15 K. (c) Mott-Schottky analysis at 1 kHz for extraction of the built-in potential (V_{bi}).

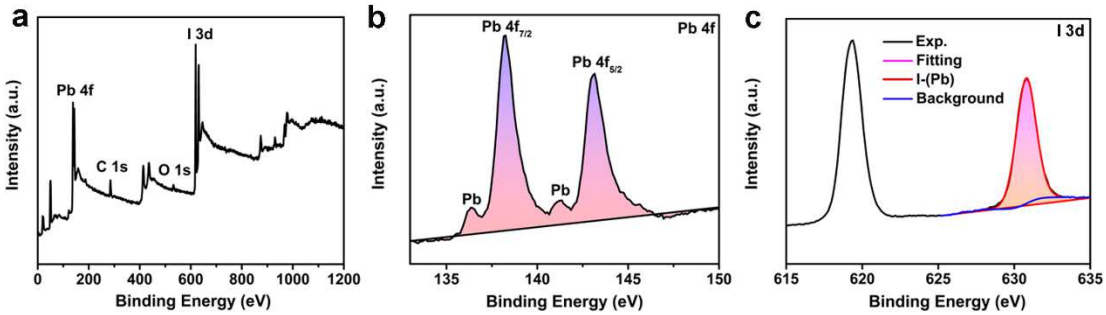

Figure S23. XPS spectrum of PbI_2 powder (a), high-resolution XPS spectra of Pb 4f (b) and I 3d (c).

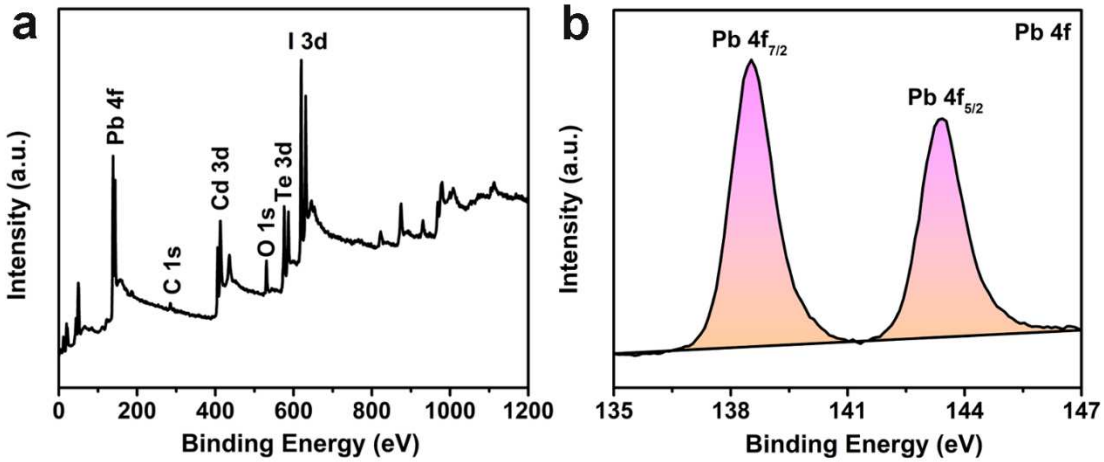

Figure S24. XPS spectrum of CdTe nanocrystals-PbI_2 (a), high-resolution XPS spectra of Pb 4f (b). In order to confirm the interaction between CdTe and PbI_2, an excess of CdTe nanocrystals powder and PbI_2 (molar ratio: 3:1) were mixed together in DMF with continuous stirring at 55°C for 2h. The products were washed with toluene for several times and were finally dried under a vacuum for further characterizations.

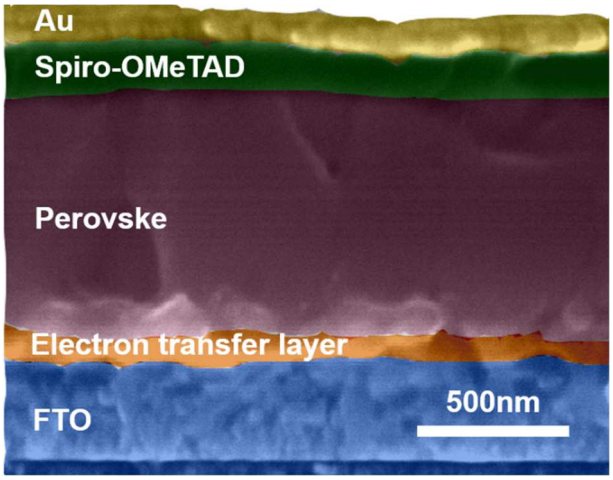

Figure S25. Cross-sectional SEM image of device upon the best ETLs.

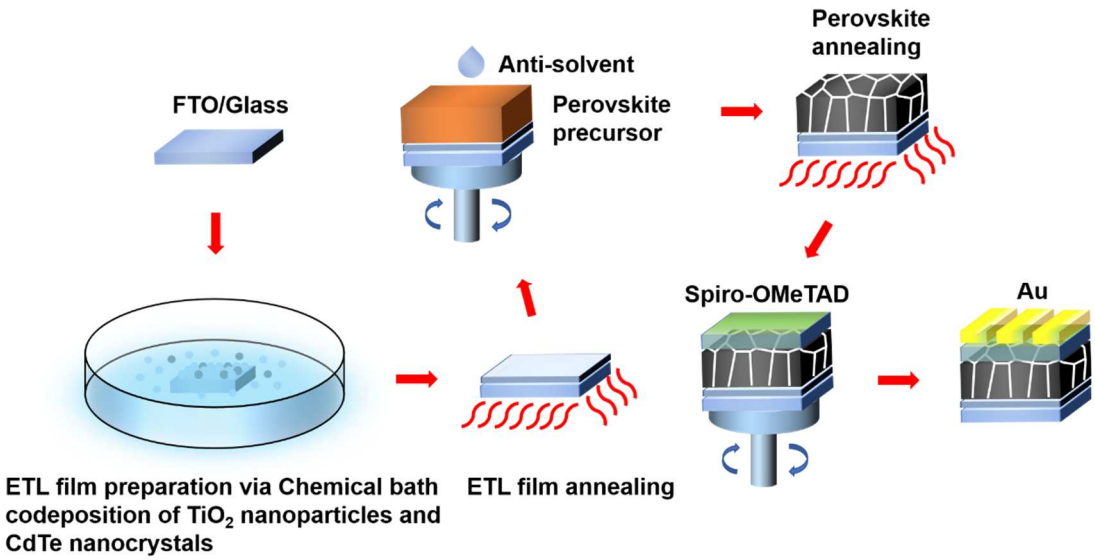

Figure S26. Schematic illustration for fabrication process of devices based on CdTe nanocrystals embedded ETLs.

Table S4. Performance parameters of champion devices upon different TiO_2 layers obtained from the J-V curves measured both in reverse scan and forward scan.

Scanning direction	*Voc* (V)	*Jsc* (mA/cm^2)	FF (%)	PCE (%)
Reverse 6%-CdTe-TiO_2	1.191	23.76	77.74	22.00
Forward 6%-CdTe-TiO_2	1.172	23.77	78.27	21.80
Reverse pristine TiO_2	1.149	22.81	76.52	20.05
Forward pristine TiO_2	1.141	22.87	67.02	17.49

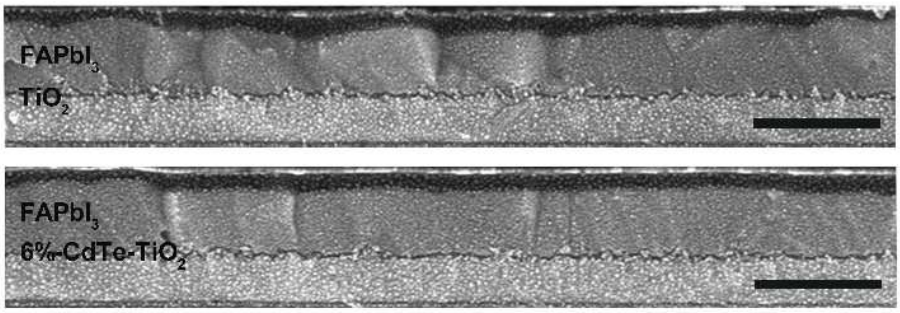

Figure S27. Cross-sectional SEM images of $FAPbI_3$ based devices with the pristine TiO_2 and 6%-CdTe-TiO_2 layer. Scale bars: 1 μm.

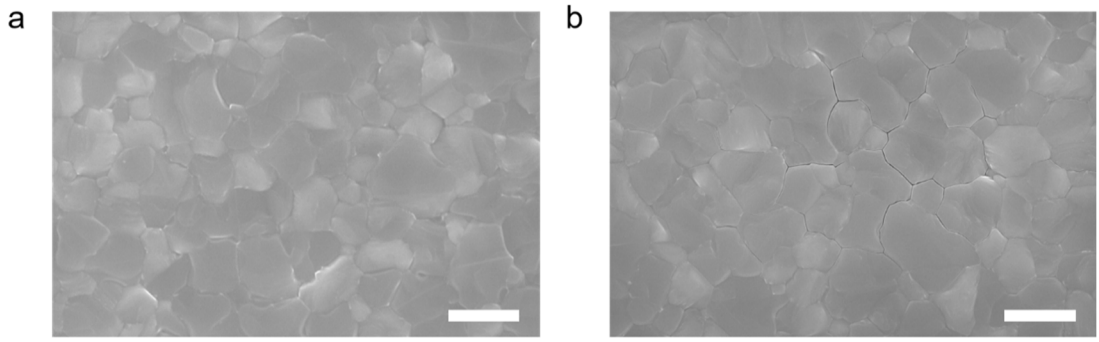

Figure S28. SEM images of $FAPbI_3$ perovskite based on the pristine TiO_2 (a) and 6%-CdTe-NCs-TiO_2 (b) layers. Scale bars: 2 μm.

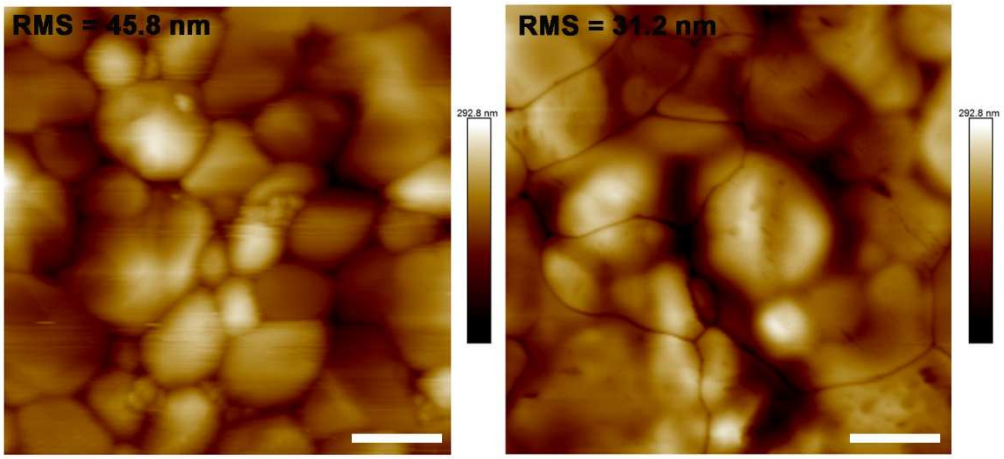

Figure S29. AFM images of $FAPbI_3$ perovskite based on the pristine TiO_2 a) and 6%-CdTe-TiO_2 b) layers. Scale bars: 1 μm.

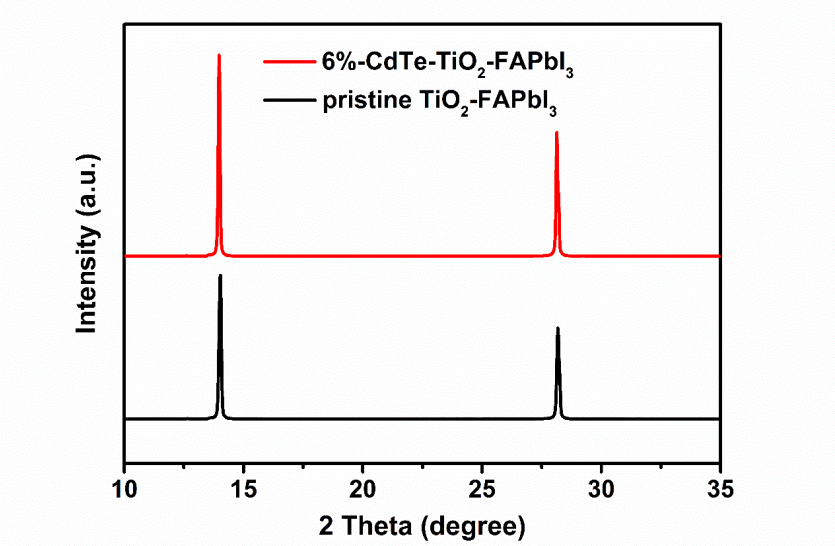

Figure S30. XRD pattern of $FAPbI_3$ upon different TiO_2 layers.

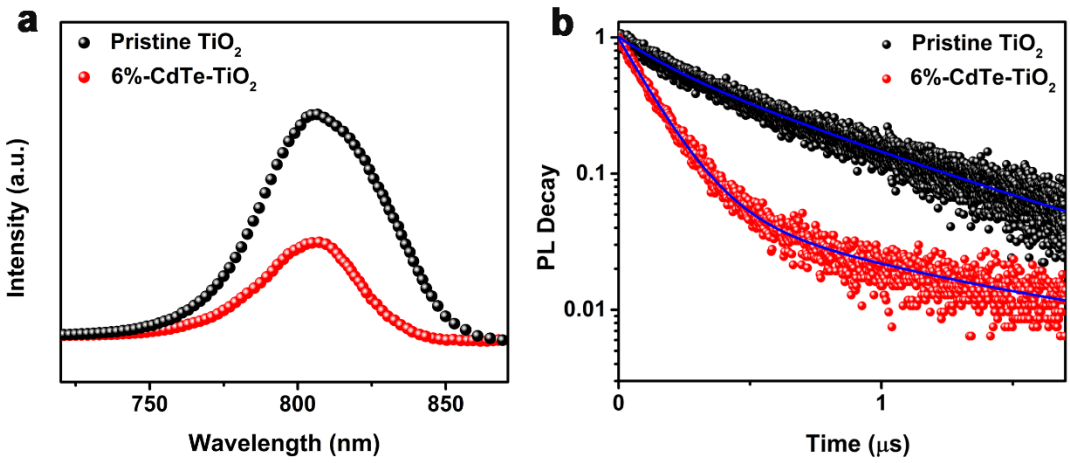

Figure S31. PL (a) and TRPL (b) spectra of $FAPbI_3$ perovskite based on the pristine TiO_2 and 6%-CdTe-TiO_2 layers.

Table S5. Summaries of fitting parameters for TRPL spectra with a structure of $FAPbI_3$/TiO2 (with and without CdTe nanocrystals)/FTO substrates.

ETLs	A_1	τ_1 (ns)	A_2	τ_2 (ns)	τ_{ave} (ns)
Pristine TiO_2	0.20	175.43	0.80	1212.01	1175.81
6%-CdTe-TiO_2	0.25	123.40	0.75	781.76	748.85

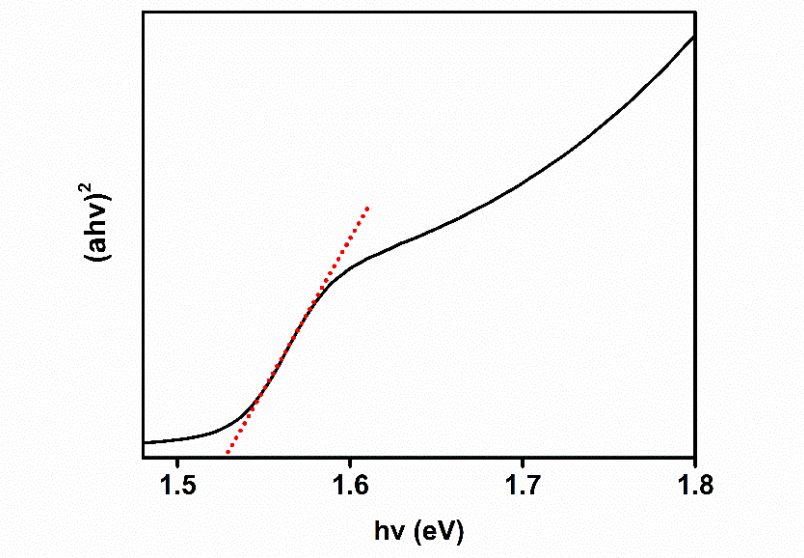

Figure S32. The Tauc plot of $FAPbI_3$ film for obtaining band gap.

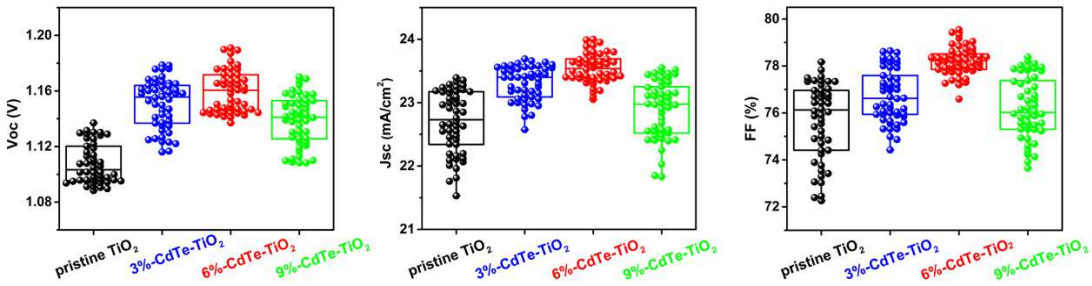

Figure S33. Statistical distributions of the photovoltaic parameters including *V*oc, *J*sc and FF for CsFAMA devices upon different TiO_2 layers. The statistics of PCEs for 50 devices is shown in Figure 4f, which exhibit an excellent reproducibility of the performance improvement with the construction of CsFAMA/CdTe-TiO_2. The average PCE rises from 18.95% to 21.23%, with *V*oc from 1.108 to 1.160 V, the average *J*sc from 22.70 to 23.54 mA/cm^2, and the FF from 75.71 to 78.21%. It is obvious that all the parameters, have been improved possibly owing to the better film quality and excellent electronic structure in CsFAMA/CdTe-TiO_2 devices.

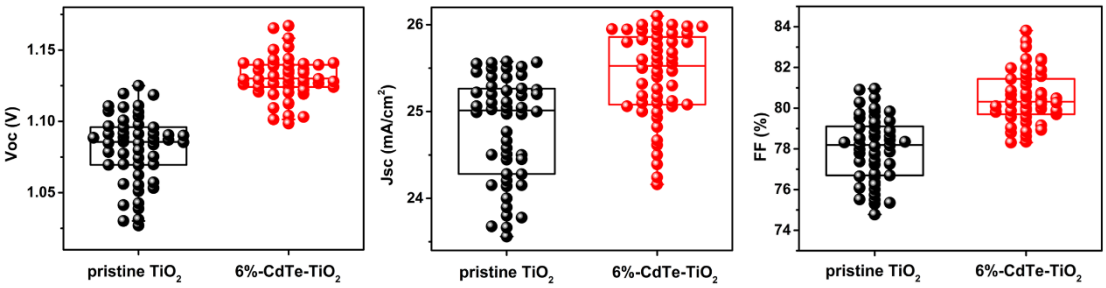

Figure S34. Statistical distributions of the photovoltaic parameters including *V*oc, *J*sc and FF for $FAPbI_3$ devices upon different TiO_2 layers. The statistics of PCEs for 50 devices is shown in Figure 4f, which exhibit an excellent reproducibility of the performance improvement with the construction of $FAPbI_3$/CdTe-TiO_2. The average PCE increases from 21.36% to 23.81%, with *V*oc from 1.081 to 1.131 V, the average *J*sc from 24.81 to 25.41 mA/cm^2, and the FF from 78.01 to 80.53%.

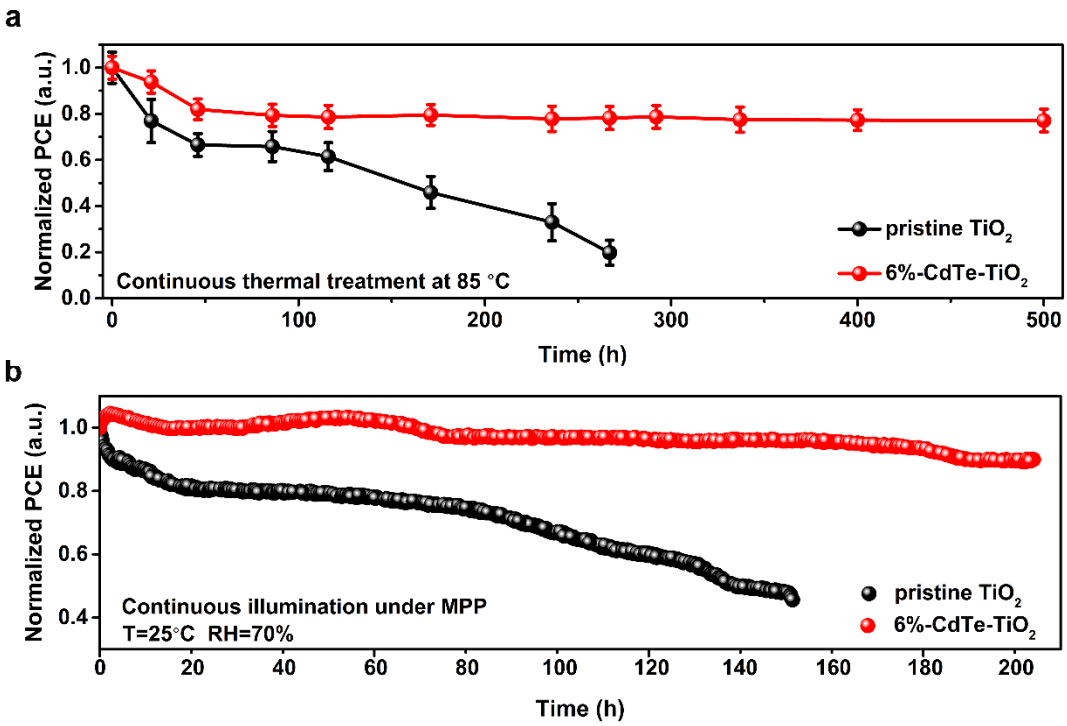

Figure S35. The long-term thermal (a) and operational (b) stability of CsFAMA-based devices with and without CdTe nanocrystals embedding. The target devices exhibit excellent thermal stability with PCE degradation of less than 20% in contrast with that of control devices (over 80%) after continuous thermal treatment of 85 °C for 500 h, as well as operational stability by retaining 90% of initial PCE over 200 h in contrast with that of control devices (approximately 40% over 150 h) at MPP tracking under full-sun illumination (AM 1.5G) in ambient air with RH of 70%.

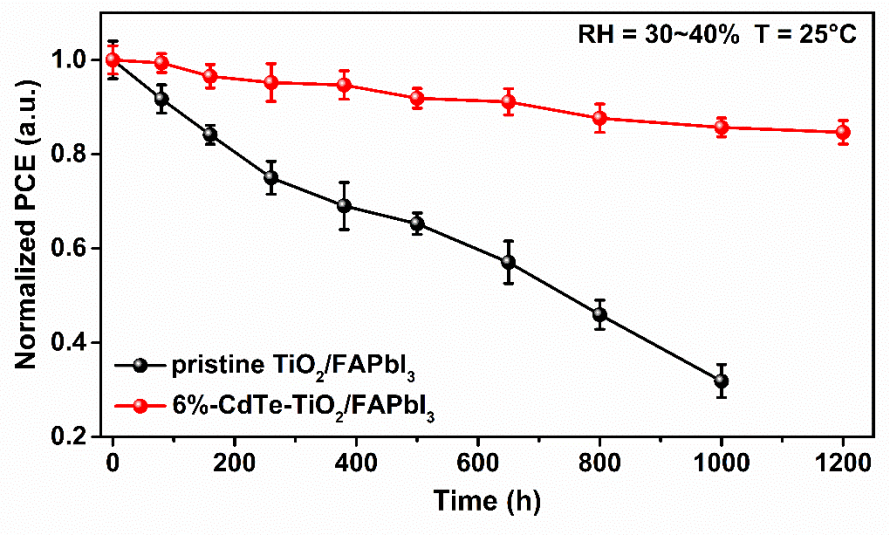

Figure S36. The long-term humidity stability of $FAPbI_3$-based devices with and without CdTe nanocrystals embedding.

Table S6. Reported values for the conductivity of different planar TiO_2 ETLs.

Type	Device structure	Best PCE (%)	Electron Mobility/ electrical conductivity ($cm^2\ V^{-1}\ s^{-1}$/$S \cdot m^{-1}$)	Ref
Urea	ITO/TiO2-NH_2/$Cs_{0.05}(FA_{0.87}MA_{0.13})_{0.95}PbI_{2.55}Br_{0.45}$/Spiro-OMeTAD/Au	21.33	7.56×10^{-3}	[9]
Dopamine	FTO/D-TiO_2/$Cs_{0.05}FA_{0.81}MA_{0.14}PbI_{2.55}Br_{0.45}$ Spiro-OMeTAD/Au	20.93	10^{-4} ~10^{-3}	[10]
LD-TiO_2	FTO/LD-TiO_2/FAMAPbI_3/Spiro-OMeTAD/Au	24.81	4.51×10^{-5}	[11]
Boron	FTO/cp-TiO_2/TiO_2 or B-TiO_2/Spiro-OMeTAD/Au Au	20.51	1.69×10^{-4}	[6]
C-PCBA	FTO/TiO_2/C-PCBA/CsFAPb$(IBr)_3$/Spiro-OMeTAD/Au	24.80	5.76×10^{-3}	[12]
[BMIM]BF_4	FTO/TiO_2/[BMIM]BF_4/MAPbI_3/PTAA/Au	19.62	3.83×10^{-4}	[13]
CO_2-plasma	FTO/ TiO_2/CO_2-plasma/MAPbI_3/Spiro-	15.39	9.29×10^{-3}	[14]

	OMeTAD/Au			
Cl-SnO_2 QDs	FTO/SnO_2-QDs/TiO_2/Perovskite/ Spiro-OMeTAD/Au	14.90	_____	[15]
CuI	FTO/TiO_2@CuI/CsFAMA/Spiro-OMeTAD/Au	19.00	3.98×10^{-4}	[16]
Phosphorene	FTO/TiO_2/phosphorene/Perovskite/Spiro-OMeTAD/Au	17.85	_____	[17]
PDI_2	ITO/TiO2/PDI_2/$MAPbI_3$/Spiro-OMeTAD/Ag	19.84	_____	[18]
Heparin sodium	FTO/TiO_2/heparin sodium/$MAPbI_3$/Spiro-OMeTAD/Au	20.1	_____	[19]
GQD	FTO/c-TiO_2 @ GQD/$MAPbI_3$/Spiro-OMeTAD/Au	19.11	_____	[20]
GQD	FTO/c-TiO_2/GQD /$MAPbI_3$/GQD/Spiro-OMeTAD/Au	19.89	_____	[21]
CdTe nanocrystals	FTO/TiO_2@CdTe/$Cs_{0.05}(FA_{0.85}MA_{0.15})_{0.95}PbI_{2.55}Br_{0.45}$/Spiro-OMeTAD/Au	22.00	1.89×10^{-2}	Our work

CdTe nanocrystals	FTO/TiO_2@CdTe/$FAPbI_3$/Spiro-OMeTAD/Au	25.05	1.89×10^{-2}	Our work

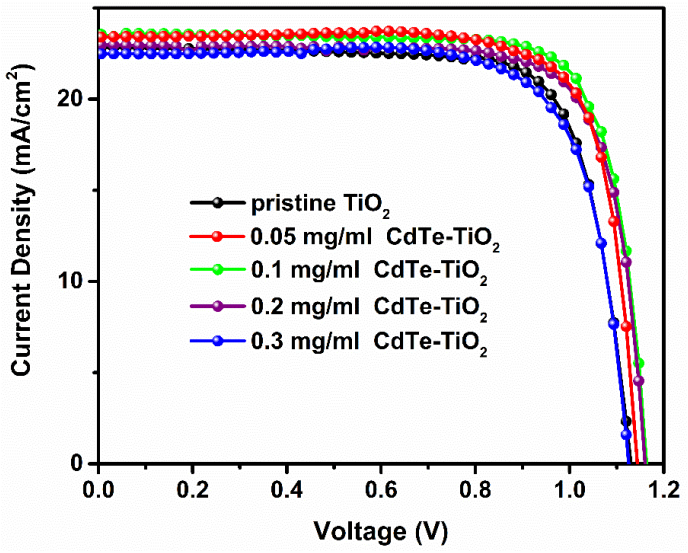

Figure S37. *J-V* curves of the CsFAMA devices based on TiO_2 layers with different concentration of CdTe nanocrystals.

Table S7. Performance parameters of champion CSFAMA devices based on CdTe@TiO_2 layers.

ETLs	Concentration of CdTe nanocrystals	*V*oc (V)	*J*sc (mA/cm^2)	FF (%)	PCE (%)
Pristine TiO_2	0 mg/ml	1.130	22.85	75.80	19.57
0.05mg/ml CdTe-TiO_2	0.05 mg/ml	1.141	23.41	78.28	20.91
0.1mg/ml CdTe-TiO_2	0.1 mg/ml	1.161	23.61	78.43	21.51
0.2mg/ml CdTe-TiO_2	0.2 mg/ml	1.158	22.97	77.50	20.61
0.3mg/ml CdTe-TiO_2	0.3 mg/ml	1.125	22.41	75.25	18.97

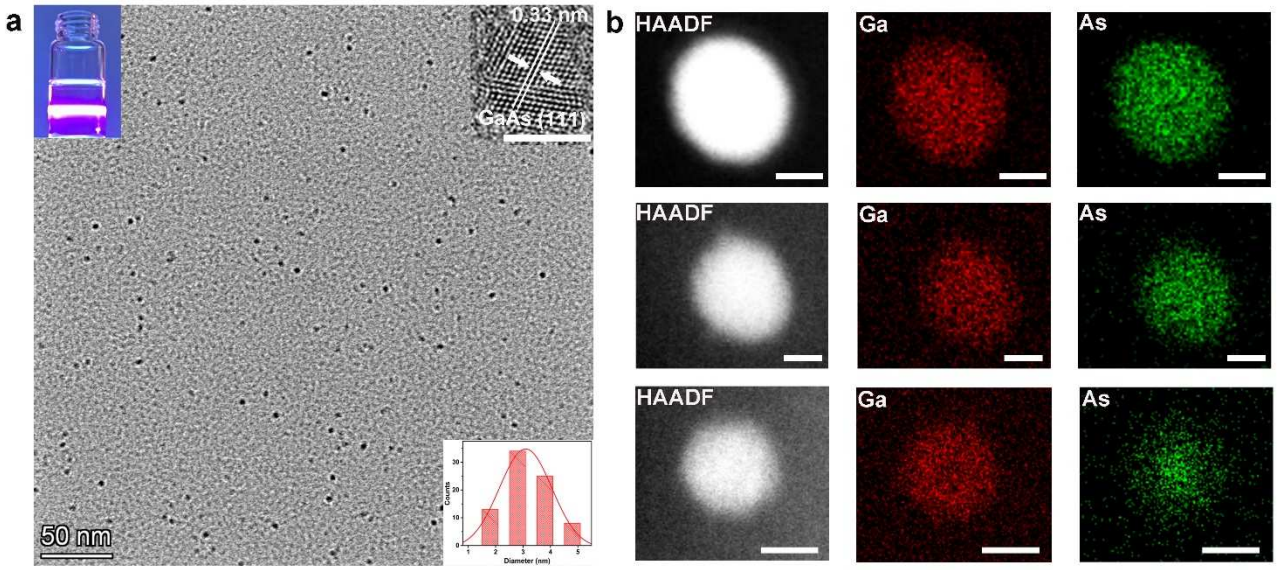

Figure S38. (a) TEM image of GaAs nanocrystals (inset: Mie-scattering image of colloids, HRTEM of GaAs nanocrystals and nanocrystals size distribution diagram,). (b) HAADF and corresponding TEM-EDS images of GaAs nanoparticles. Scale bar: (a) 50 nm, inset: 5 nm, (b) top: 10 nm, middle: 5 nm, bottom: 5 nm.

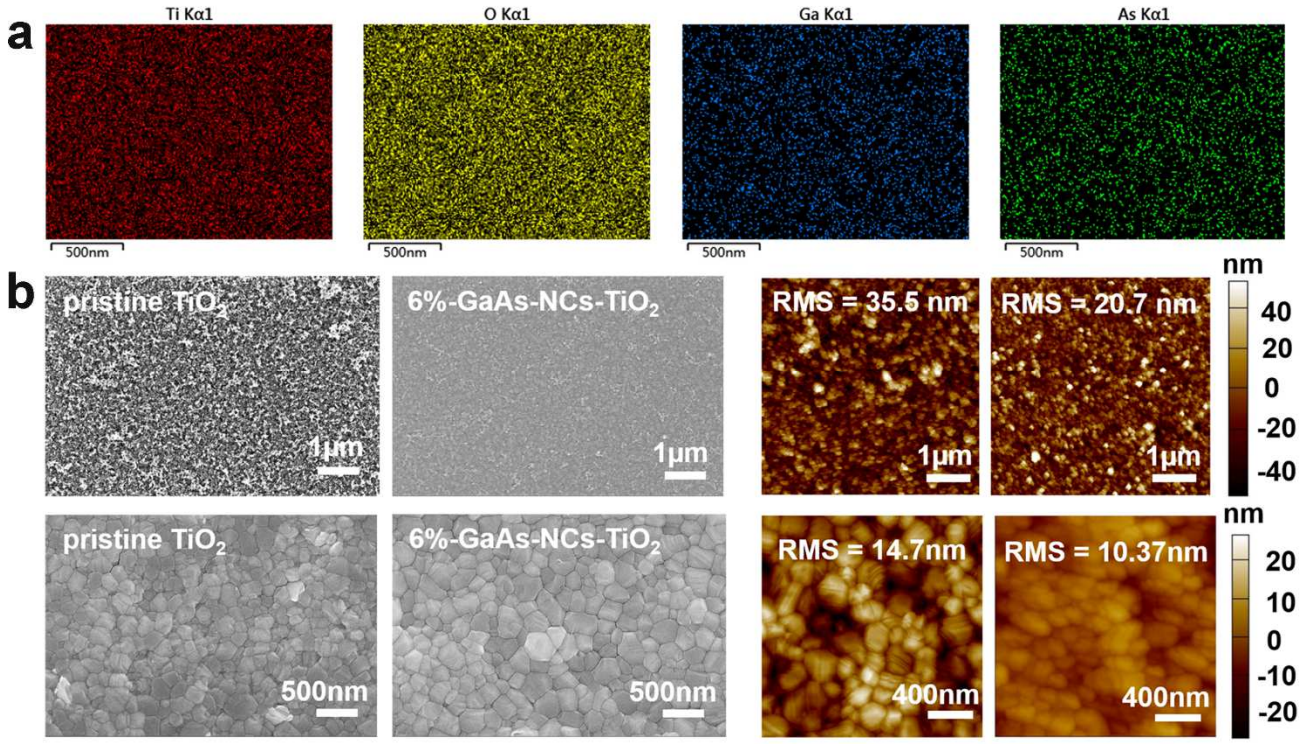

Figure S39. (a) EDS mapping images for 9%-GaAs-TiO_2 film. (b) SEM top-view images of different TiO_2 and CsFAMA perovskite films deposited on the corresponding TiO_2 films. AFM height images of different TiO_2 and CsFAMA perovskite films based the pristine TiO_2 and 6%-GaAs-NCs-TiO_2 films.

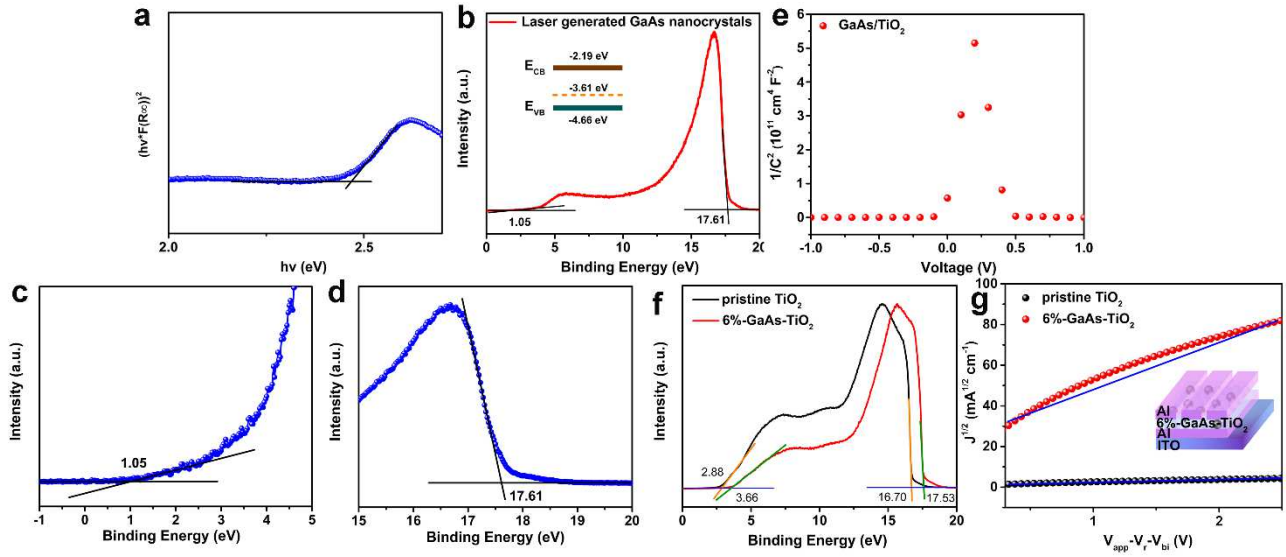

Figure S40. (a) The optical bandgaps of GaAs nanocrystals estimated by UV-visible diffuse-reflectance spectrum (UV-Vis DRS); (b) UPS spectrum of GaAs nanocrystals with UPS Fermi edge (c) and the cut-off energy (d); (e) Mott-Schottky plots of GaAs nanocrystals embedded TiO_2 matrix; (f) UPS spectra of different TiO_2 films with and without GaAs nanocrystals embedding; (g) Electron mobilities of different ETL using the SCLC model, and the inset shows the device structure of ITO/Al/6%-GaAs-TiO_2/Al.

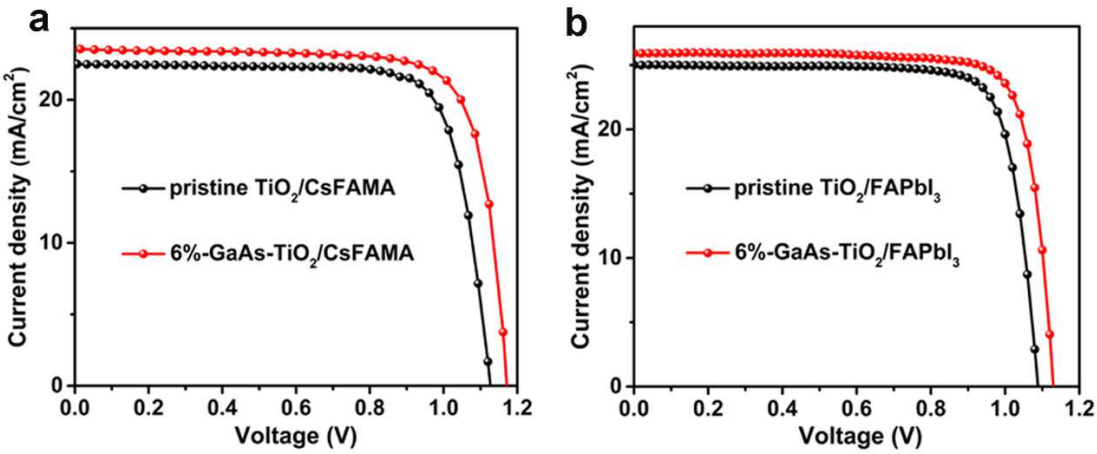

Figure S41. (a) *J-V* curves of CsFAMA-based devices with and without GaAs embedding. (b) *J-V* curves of $FAPbI_3$-based devices with and without GaAs embedding.

Table S8. Performance parameters of champion devices upon the pristine and 6%-GaAs-NCs-TiO_2 layers.

ETLs	*V*oc (V)	*J*sc (mA/cm^2)	FF (%)	PCE (%)
pristine TiO_2/CsFAMA	1.126	22.50	77.83	19.73
6%-GaAs-TiO_2/CsFAMA	1.172	23.60	77.89	21.54
pristine TiO_2/$FAPbI_3$	1.089	25.00	80.29	21.86
6%-GaAs-TiO_2/$FAPbI_3$	1.130	25.65	81.05	23.49

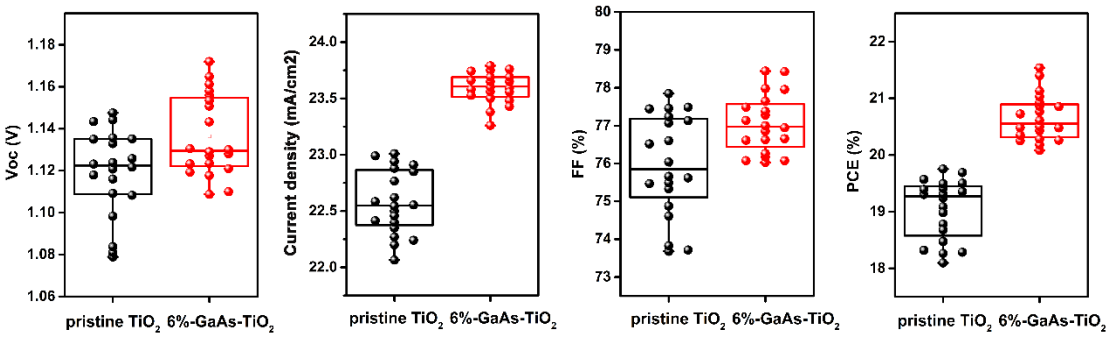

Figure S42. The distribution of photovoltaic parameters for CsFAMA-based devices with and without GaAs embedding.

Reference:

[1] Luan, Y. et al. High-performance planar perovskite solar cells with negligible hysteresis using 2,2,2-trifluoroethanol-incorporated SnO_2. *iScience* **16**, 433-441 (2019).

[2] Zeng, C., Ramos-Ruiz, A., Field, J. A. & Sierra-Alvarez R. Cadmium telluride (CdTe) and cadmium selenide (CdSe) leaching behavior and surface chemistry in response to pH and O_2. *J. Environ. Manage.* **154**, 78-85 (2015).

[3] Wang, K. et al. CO_2 plasma-treated TiO_2 film as an effective electron transport layer for high-performance planar perovskite solar cells. *ACS Appl. Mater. Interfaces* **9**, 33989-33996 (2017).

[4] Yang, D. et al. High efficiency planar-type perovskite solar cells with negligible hysteresis using EDTA-complexed SnO_2. *Nat. Commun.* **9**, 3239 (2018).

[5] Tan, H. et al. Efficient and stable solution-processed planar perovskite solar cells via contact passivation. *Science* **355**, 704-705 (2017).

[6] Shi, X. et al. Enhanced interfacial binding and electron extraction using boron-doped TiO_2 for highly efficient hysteresis-free perovskite solar cells. *Adv. Sci.* **6**, 1901213 (2019).

[7] Bai, D. et al. Interstitial Mn^{2+}-driven high-aspect-ratio grain growth for low-trap-density microcrystalline films for record efficiency $CsPbI_2Br$ solar cells. *ACS Energy Lett.* **3**, 970-978 (2018).

[8] Li, N. et al. Cation and anion immobilization through chemical bonding enhancement with fluorides for stable halide perovskite solar cells. *Nat. Energy* **4**, 408-415 (2019).

[9] Hu W*, et al.* Low-Temperature In Situ Amino Functionalization of TiO2 Nanoparticles Sharpens Electron Management Achieving over 21% Efficient Planar Perovskite Solar Cells. *Adv. Mater.* **31**, 1806095 (2019).

[10] Zhang Y*, et al.* Dopamine-crosslinked TiO2/perovskite layer for efficient and photostable perovskite solar cells under full spectral continuous illumination. *Nano Energy* **56**, 733-740 (2019).

[11] Huang H*, et al.* 24.8%-efficient planar perovskite solar cells via ligand-engineered TiO2 deposition. *Joule* **6**, 2186-2202 (2022).

[12] Chen Z*, et al.* Reconfiguration toward Self-Assembled Monolayer Passivation for High-Performance Perovskite Solar Cells. *Adv. Energy Mater.* 2202799 (2022).

[13] Yang D*, et al.* Surface optimization to eliminate hysteresis for record efficiency planar perovskite solar cells. *Energy Environ. Sci.* **9**, 3071-3078 (2016).

[14] Wang K*, et al.* CO_2 Plasma-treated TiO_2 film as an effective electron transport layer for high-performance planar perovskite solar cells. *ACS Appl. Mater. Interfaces* **9**, 33989 (2017).

[15] Wu, T. *et al.* Chlorine capped SnO_2 quantum dots modified TiO_2 electron selective layer to enhance the performance of planar perovskite solar cells. *Sci. Bull.* 64, 547-552 (2019).

[16] Byranvand, M. M., Kim, T., Song, S., Kang, G., Ryu, SU. & Park, T. p-Type CuI islands on TiO_2 electron transport layer for a highly efficient planar-perovskite solar cell with negligible hysteresis. *Adv. Energy Mater.* **8**, 1702235 (2018).

[17] Batmunkh M*, et al.* Efficient production of phosphorene nanosheets via shear stress mediated exfoliation for low-temperature perovskite solar cells. *Small Methods* **3**, 1800521 (2019).

[18] Yang, L. *et al.* Restrained light-soaking and reduced hysteresis in perovskite solar cells employing a helical perylene diimide interfacial layer. *J. Mater. Chem. A* **6**, 10379-10387 (2018).

[19] You S*, et al.* A biopolymer heparin sodium interlayer anchoring TiO_2 and $MAPbI_3$ enhances trap passivation and device stability in perovskite solar cells. *Adv. Mater.* **30**, 1706924 (2018).

[20] Ryu, J. et al. Size effects of a graphene quantum dot modified-blocking TiO_2 layer for efficient planar perovskite solar cells. *J. Mater. Chem.* A **5**, 16834-16842 (2017).

[21] Zhang, X. et al. Graphdiyne quantum dots for much improved stability and efficiency of perovskite solar cells. *Adv. Mater. Interfaces* **5**, 1701117 (2018).